



**Repositorio Institucional de la Universidad Autónoma de Madrid**

<https://repositorio.uam.es>

Esta es la **versión de autor** del artículo publicado en:

This is an **author produced version** of a paper published in:

Clay Minerals 2<sup>nd</sup> July (2018): 1-32

**DOI:** <http://doi.org/10.1180/clm.2018.16>

**Copyright:** © Mineralogical Society of Great Britain and Ireland 2018

El acceso a la versión del editor puede requerir la suscripción del recurso

Access to the published version may require subscription

# Low-pH cement mortar-bentonite perturbations in a small-scale pilot laboratory experiment

D.E. González-Santamaría, M. Angulo, A.I. Ruiz, R. Fernández, A. Ortega, J. Cuevas\*

*Departamento de Geología y Geoquímica, Facultad de Ciencias. Universidad Autónoma de Madrid. Cantoblanco s/n. 28049*

*Madrid, Spain. [jaime.cuevas@uam.es](mailto:jaime.cuevas@uam.es)*

**ABSTRACT:** A novel method to perform small-scale laboratory experiments that reproduce concrete-bentonite and concrete-groundwater interactions has been developed. These interfaces will prevail in engineered barrier systems used for nuclear waste isolation. With the goal of optimizing the experimental method, this work has analysed the geochemical interaction of distilled water, low-pH cement mortar and FEBEX-bentonite for 75 days. Limited but evident material reactivity has been identified, mainly decalcification in cement mortar, carbonation at the interface with bentonite and Mg enrichment in bentonite. These results are consistent with the state-of-the-art literature reviewed and used to validate this small-scale pilot laboratory experiment to establish the basis for further studies comparing the behaviour of different buffer and cement materials.

**Keywords:** Radioactive waste confinement, alkaline alteration, low-pH cements, bentonite, laboratory experiments.

## INTRODUCTION

The present and future management of high-level radioactive waste (HLRW) is one of the major environmental issues, especially considering its long radiotoxicity ( $10^4$ - $10^6$  years). Currently, the deep geological repository (DGR) is the most accepted management option for HLRW long-term isolation (NEA-OECD, 2003; U.S. DOE, 2014). Within the European

Union, Finland, Sweden and France are expected to approve a final DGR location before 2020 (Gibney, 2015; Ewing *et al.*, 2016). The DGR concept is based on a multibarrier system (engineered barrier system, EBS) to delay and avoid the release of radionuclides into the biosphere. A generic EBS constructed in a granitic host rock formation consists of the following:

- 1) A metallic canister as a first barrier in contact with the radioactive waste.
- 2) A clay barrier surrounding the canister.
- 3) Concrete to seal and close the galleries.

The clay barrier acts as both a hydraulic seal and a physical-chemical buffer. Bentonite is a swelling clay material that has been selected by most of the waste management organizations (IAEA, 2013; NEA-OECD, 2003) as an optimal material for the backfilling and sealing of HLRW repositories due to its low permeability, low diffusivity, high retention of cations and swelling capacity (Meunier *et al.*, 1998; Kaufhold *et al.*, 2013; Gómez-Espina & Villar, 2016; Kaufhold & Dohrmann, 2018). Concrete and bentonite will be in close contact, and they will interact within each other. In addition, the EBS system will be in contact with flowing groundwater in the host rock, which will affect the long-term safety in case degradation processes develop. In the long term, the interaction among water, concrete and clay will generate an indeterminately complex chemical system that could compromise the storage security (Savage, 2014). Furthermore, its evolution will vary depending on the type of cement and clay used as a barrier (Dauzères *et al.*, 2010; Jenni *et al.*, 2014). Thus, understanding the degradation pathways due to barriers and groundwater interactions and clarifying the critical parameters involved herein are of fundamental interest to advance the DGR design. Conventional Portland type cementitious materials generates an alkaline fluid ( $\text{pH} > 13$ ) caused by the dissolution of alkali hydroxides and  $\text{Ca}(\text{OH})_2$  (portlandite) in the pore water of the cement matrix, which can attack smectite crystal lattices in neighbouring clay seals (Liu *et al.*, 2014). Therefore, the hyperalkaline front could modify the smectite mineralogy and its properties. Previous investigations have analysed the behaviour of different clays in contact with the hyperalkaline front. However, the concrete should not be only simulated by a high-pH solution in equilibrium with  $\text{Ca}(\text{OH})_2$  ( $\text{pH} = 12$ ) or alkali hydroxides (Bildstein & Claret 2015), omitting the chemical and mineralogical evolution of the concrete itself. Some authors

have outlined the relative absence of representative experiments in real clay/concrete interfaces (Gaboreau *et al.*, 2011; Gaboreau *et al.*, 2012; Bartier *et al.*, 2013; Mäder *et al.*, 2017) and the difficulty to take into account the effects of real volumes and the composition of solutions migrating through connected porosities (Cuevas *et al.*, 2016). Moreover, few works have put low-pH cementitious materials in contact with clays (Jenni *et al.*, 2014; Dauzères *et al.*, 2016; Lerouge *et al.*, 2017). To avoid extreme alkalinity, experiments have been carried out with low-pH cement mortars ( $\text{pH} < 12$ ). Several studies suggest that low-pH cement-based materials have insignificant effects on clay structures (Bäckblom, 2005; Berner *et al.*, 2013; Cuevas *et al.*, 2016), while they have demonstrated a resistance to granitic groundwater exposure (García Calvo *et al.*, 2010). However, low-pH cements have shown a lower resistance than high-pH cements to the influence of carbonated waters (Dauzères *et al.*, 2014) since some of the cement paste hydration products, such as ettringite, are more unstable (Trotignon *et al.*, 2007) and precipitate calcite and gypsum. Low-pH cement-based materials can present a carbonation process, but the high-pH cementitious materials can develop a larger protective calcium carbonate film that increases the retardation of the decalcification process, at least temporarily (Jenni *et al.*, 2014). In addition to these uncertainties, the complex structure and chemistry of the mineral phases formed during the alkaline perturbation at these interfaces were unclear until a few years ago (Bildstein & Claret, 2015), but recent experiments have examined and provided new characterizations of their structure and chemistry (Roosz *et al.*, 2015; Nied *et al.*, 2016; Lerouge *et al.*, 2017). This might be the case for mineral phases such as magnesium silicate hydrates (M-S-H) or calcium aluminium silicate hydrates (C-A-S-H; Lothenbach *et al.*, 2015). It is known that concrete composition comprises a wide range of mineral phases, such as calcium silicate hydrates (C-S-H) with different Ca/Si ratios and aluminate-, calcium- and sulphate-bearing phases such as ettringite and calcium monosulphate-aluminate hydrate (CmSAH; Van Damme & Pellenq, 2013). Experimental research on C-S-H in low-pH concretes is sparse, and their parameters of formation and stabilization are not yet sufficiently known to ensure a feasibility assessment.

In this context, small-scale laboratory experiments could be interesting because they approach real conditions through a simplified system, facilitating the control of different parameters and allowing the assessment of the different possible conditions

64 expected in a DGR. These experiments may provide reaction pathways on a short time scale, making them useful tools as  
65 sources of data for geochemical modelling. In addition, they can complement other types of experiments, such as batch  
66 experiments or large *in situ* underground laboratory experiments. Consequently, the aim of this study was the development and  
67 optimization of a new representative small-scale laboratory experiment able to reproduce the contact between concrete and  
68 bentonite that would occur in a DGR and, at the same time, to test procedures and methods for assessing and describing the  
69 geochemical perturbations under different conditions.

## 71 MATERIALS AND METHODS

### 72 *Experimental setup and characterization techniques*

73 The pilot experiment was performed using distilled water, simulating diluted granitic groundwater, low-pH cement mortar and  
74 FEBEX-bentonite as the reference Spanish bentonite for the DGR. The experiment was run for 75 days under isothermal  
75 conditions ( $25 \pm 5$  °C), based on the range of temperatures expected at the concrete-bentonite interface according to the data  
76 provided by Villar *et al.* (2012) for a FEBEX *in situ* experiment after 13 years for a sealing concrete plug in a granitic DGR.  
77 The low-pH cement mortar and the compacted FEBEX-bentonite clay were placed in a 4 mm thick methacrylate sleeve confined  
78 by two stainless steel cylindrical caps (Fig. 1). The cell dimensions are 20 mm in internal diameter and 9 mm in height for each  
79 material (18 mm in total). The objective of the design of these cells included the minimization of undesirable effects during the  
80 dismantling of the cells for further solid characterization, such as the tedious separation of cement mortar and bentonite from  
81 the carcass and the creation of fractures or deformations in both materials, avoiding the interaction of the materials with the  
82 atmosphere. Therefore, it was necessary to design a compact external stainless-steel case (together with connections and filters)  
83 able to resist the high-pressure conditions (1-5 MPa) caused by the hydration of bentonite (Villar & Lloret, 2004). The setup of  
84 columns also involved two porous steel filters that allowed pressurized water infiltration. The constant hydraulic head of the

distilled water was fixed to 1 MPa by an automatic piston pump (Gilson 307) model and carried through PEEK tubes. The generated cement mortar-bentonite interface (hereinafter referred to as the C-B interface) and the cement mortar-distilled water interface (hereinafter referred to as the C-W interface) were separated by a 0.45 µm polytetrafluoroethylene (PTFE) membrane to facilitate the separation of materials and the access to both interfaces. The infiltrated water was collected in a syringe for the aqueous phase survey. This effluent was subjected to the determination of the following: (i) alkalinity using a Metrohm 888™ potentiometric titrator, (ii) silica by spectrophotometric determination of molybdate-reactive silica in the effluent using a Milton Roy Spectronic® instrument at a wavelength of 825 nm, and (iii) major chemical ions by ion chromatography coupled to a conductivity detector using a Metrohm 802 compact IC plus model.

The hydraulic conductivity ( $k$ ) was calculated by Darcy's law using formula (1):

$$Q = k/A * \Delta h / \Delta L \quad (1)$$

where

$Q$  = the quantity of water leached over the time  $t$  (m<sup>3</sup>/s);  $k$  = hydraulic conductivity (m/s);  $A$  = cross-sectional area (m<sup>2</sup>);  $\Delta h$  = hydraulic head (m); and  $L$  = column length.

The solid phase characterization was performed by X-ray diffraction (XRD), grazing incidence X-ray diffraction (GI-XRD) and a scanning electron microscope attached to an energy dispersive X-ray analyser (SEM-EDX). The mineral identification by XRD was performed on bulk, randomly oriented cement mortar and bentonite powders using a  $\theta/2\theta$  X'Pert PANalytical instrument with an X'Celerator detector. XRD patterns were recorded in an angular range ( $2\theta$ ) of 3-70°. This method allowed measurements equivalent to 0.016° angular steps for 100 s at each step. The voltage and intensity of the operated X-ray Cu tube were 45 kV and 40 mA, respectively. To perform the GI-XRD analyses, angles of 1°, 5° and 8°  $2\theta$  were used with 0.04° and 2 seconds of angular step and time step increases, respectively. The SEM-EDX equipment was a Hitachi S-3000N scanning electron microscope coupled to an INCAx-sight Oxford Instruments™ energy dispersive X-ray analyser.

106 The EDX quantification was performed by means of internal standard semi-quantitative analyses.

107 Semi-quantitative EDX elemental composition analysis was performed for the following reasons: (1) to determine the elemental  
108 composition variations along a linear transect through the whole cement-mortar/bentonite composite probe, taken from the  
109 hydration mortar face to the porewater outflow at the end of the compacted bentonite, and (2) to perform localized punctual  
110 analyses to describe either the chemistry of the cement mortar matrix for the intergranular zones between the quartz grains or  
111 the discrete mineral phase compositions where singular morphologies (crystals, polycrystalline aggregate-defined  
112 morphologies) were distinguished. To evaluate the quality of these results, EDX spectra of a heterogeneous 300 x 200  $\mu\text{m}$  area,  
113 typical of the analysis performed on the linear transect in the cement mortar, were acquired using several integration times, from  
114 10 s to 80 s, at 5 s intervals. The % deviation was calculated as 100 times the ratio of the standard deviation to the determined  
115 % chemical element value. For major elements in the concrete (Al, Si and Ca), instrumental % deviations, obtained by taking  
116 their average value in the 30-50 s interval, were less than 10 %, related to their concentration being lower for silicon (< 1 %)  
117 and higher for Al (9 %) (Table 1). The % deviation from measured values, however, was less than 6 % for the average  
118 measurement value. For elements that have contents within 1-5% (K, Fe), the % deviation from the average of the measured  
119 values was typically 10-15 %. Forty seconds was considered enough time to not compromise the analysis quality and to avoid  
120 excessively time-consuming data acquisition. In terms of the punctual analyses, with a typical 5 x 5  $\mu\text{m}$  spot, the analysis data  
121 for a needle-like ettringite polycrystalline aggregate are shown in Table 1. In general terms, the atomic ratios obtained,  
122 considering that some impurities are always present (Si-phases and carbonates), are within 10-15 % deviation using theoretical  
123 values for ettringite.

124  
125 *FEBEX-bentonite*

The experiments have been performed with FEBEX-bentonite from the Cortijo de Archidona deposit (Almería, Spain; Caballero *et al.*, 2005). The physical-chemical properties of the FEBEX-bentonite, as well as its most relevant thermo-hydro-mechanical and geochemical properties, have been extensively studied and published elsewhere (e.g., ENRESA, 2006). The FEBEX-bentonite was compacted with its hygroscopic water content (13 %) at room conditions ( $23 \pm 1$  °C) and at a nominal dry density of  $1.60 \text{ g/cm}^3$ . Finally, the bentonite was placed inside the methacrylate sleeve (Fig. 1).

#### *Low-pH cement mortar*

The low-pH cement binder was prepared with ordinary Portland cement (OPC) CEM I 42.5 R SR mixed with silica fume (SF) (OPC [60 wt.%] + SF [40 wt.%]). Both materials were provided by the Eduardo Torroja Institute for Construction Science from CSIC (Spanish National Research Council). Subsequently, a 0.42 ratio of distilled water/binder and a 1:3 ratio of binder/silica sand (grain size  $< 1 \text{ mm}$ ) were added. The fresh low-pH cement mortar obtained was pressed inside the methacrylate sleeve and covered by the PTFE membrane. After the bentonite was compacted to fill the whole sleeve, the cement mortar was stored in a hydration chamber and exposed to a water-saturated atmosphere for 90 days. The low-pH cement mortar chemical composition (Table 2) and the composition of major ions in the pore solution after 90 days of curing time (presumably at equilibrium) were provided by García Calvo (2012; Table 3). To obtain an initial reference sample, a slice of the initial low-pH cement mortar was cut, polished and characterized by SEM-EDX. The pH measured in the pore solution of the initial low-pH cement mortar (Table 3) was obtained following the leached ex situ method (García Calvo, 2012). The XRD powder patterns and GI-XRD showed the absence of portlandite [ $\text{Ca}(\text{OH})_2$ ] and the presence of C-S-H together with characteristic clinker phases that were not yet hydrated (Fig. 2). SEM images showed homogeneously distributed grains of silica sand within the cement matrix (Fig. 3a). Additionally, the reference low-pH cement mortar showed the presence of non-reacted silica fume grains that indicate incomplete dispersion. Nevertheless, the conversion of portlandite to C-S-H was fully completed. The EDX analyses were conducted considering only the cement matrix and taking a representative number of analyses, where silica grains were



intentionally avoided. Under these conditions, a Ca/Si ratio of  $0.9 \pm 0.1$  was obtained, representative of the cement matrix composition (based on 14 analyses; see the detail of the spot size selected in Fig. 3a; a supplementary file named Table S1 with data of the EDX chemical analysis is provided. It has been deposited with the Editor in Chief and are available from <http://www.clays.org/Journal/JournalDeposits.html>). This result can be applied to the C-S-H composition present in the reference low-pH cement mortar since C-S-H are the main and almost unique hydrated phases present in the binder (García Calvo *et al.*, 2012). The determined Ca/Si ratios are in agreement with the previous studies of Stronach & Glasser (1997). These authors indicated that to obtain a low pH in the cement materials, the Ca/Si ratio must be lower than 1.1. Additionally, it must be noted that the silica content in these ratios could be overestimated due to the presence of small microsilica particles (silica fume) (García Calvo *et al.*, 2010). In the punctual analysis, morphologies typical of ettringite were observed in local regions (Fig. 3b). EDX chemical analyses corroborate the identification of such mineral phases ( $Al/S = 0.8$ ; theoretical  $Al/S = 0.67$ ), although they cannot be detected and quantified in our XRD patterns.

#### *Dismantling, cutting and sampling*

After 75 days of reaction, the cement mortar-bentonite column was dismantled and divided in subsamples using a Well®2000 cutting machine model with a diamond wire saw. Different subsamples were sliced from the initial column (Fig. 4). The number of subsamples and their sizes were determined by the quantity needed to carry out the post-mortem analyses.

A half-sample of the cement mortar-bentonite column was divided in two: one quarter was used to perform XRD and SEM-EDX analyses, and the other quarter was used to perform GI-XRD analyses. All analyses were performed to study the influence between both materials and the effects of the water flow. The subsample prepared for XRD and SEM-EDX analyses was sliced into 6 new subsamples, with a 3 mm thickness for each portion, parallel to the interface (as shown in Fig. 4). The segmentation potentially permitted the study of perturbations as a function of distance from the interface (3, 6 and 9 mm) and then the

assessment of the spatial progress of the geochemical reactions. Finally, prior to performing the analyses, these subsamples were dried in a vacuum chamber.

The other half-sample was used for optical inspection to analyse a longitudinal chemical profile of the elemental distribution along the column axis measured by SEM-EDX and was used to carry out spot EDX analyses on the cement matrix near the C-W interface and C-B interface. This profile sample was freeze dried in liquid nitrogen, dried under vacuum in a  $P_2O_5$ -dehydrated atmosphere until  $10^{-4}$  Pa and polished up to 2500 grit sheet sandpaper.

The chemical profile was obtained by SEM-EDX analyses in selected areas. Using the C-B interface as a reference, EDX measurements were conducted towards the bentonite end of the column and towards the interface with the infiltrating water solution (C-W interface). A total of 10 analyses with rectangular dimensions of 10  $\mu$ m in the direction perpendicular to the C-B interface and approximately 120  $\mu$ m in the direction parallel to the C-B interface were performed. The next 5 analyses had dimensions of 100 by 300  $\mu$ m in the perpendicular and parallel directions to the C-B interface, respectively. Finally, 8 analyses towards the bentonite column end and 10 analyses towards the C-W interface of 1 by 3 mm were performed. The areas analysed are illustrated in Fig. 5.

## RESULTS

### *Aqueous phase*

The volume of aqueous solution effluent collected after 75 days was 2.03 ml. The values of major ions, alkalinity, aqueous silica and pH are shown in Table 3. According to equation (1), the calculated hydraulic conductivity was  $1.6 \times 10^{-13}$  m/s based only on one measurement.

### *General overview of the small-scale pilot laboratory experiment*

The profile sample of the post-mortem low-pH cement mortar-bentonite column is shown in the backscattered electron image in Fig. 5. The freeze-drying process, in preparation for the SEM-EDX analyses, produced a decrease in the bentonite volume and a few macroscopic cracks in the bentonite part. However, the general aspect of the bentonite texture remained homogeneous. The low-pH cement mortar showed an increased presence of air voids (Fig. 5) compared to the reference cement mortar sample (Fig. 3a), suggesting a leaching process of the cement matrix towards bentonite.

The chemical composition profiles obtained by EDX analyses illustrate the elemental distribution along the complete column axis (Fig. 6a). The main chemical perturbations are observed at the C-B interface, although a visible decrease in Ca is also observed in the cement mortar near the C-W interface.

#### *Low-pH cement mortar perturbations*

The chemical profile showed a slight decrease in the percentage of Ca over the first 3 mm from the C-W interface (Fig. 6a). Conversely, the EDX profile showed a Ca increase towards the C-B interface, and close to the C-B interface (in the range 0-100  $\mu\text{m}$ ), two peaks of Ca are observed with an associated opposite effect on the Si concentration (Fig. 6b-c). A slight increase in Al (2.5-4.0 %) is observed in the cement mortar near the C-B interface (25  $\mu\text{m}$ ), and although the increase in concentration is low, it is significant within an established 20-25 % relative error (Fig. 6c). In addition, spot SEM-EDX analyses performed on the polished cement mortar sample near the C-W interface showed Ca/Si ratios in the range of  $0.7 \pm 0.1$  (based on 8 analyses performed on selected cement matrix regions; Fig. 7a), while the spot analyses obtained near the C-B interface showed Ca/Si ratios in the range of  $0.8 \pm 0.1$  (based on 7 analyses also performed on selected cement matrix regions; Fig. 7b). Moreover, the morphologies of C-S-H (with a Ca/Si ratio = 0.6 obtained by EDX) and ettringite-like crystals (Al/S = 0.6) were found on the surface of low-pH cement in contact with only the bentonite (Fig. 8a-b). XRD analyses of the reference low-pH cement mortar sample and the post-mortem subsamples are shown in Fig. 9a-b. The XRD diffractogram shows weak changes at 3.04-3.06 Å

among the reference low-pH cement mortar and the low-pH cement mortar subsamples. Regarding the reference low-pH cement mortar, characteristic reflections of C-S-H phases (2.79 Å, 2.75 Å, 2.66 Å and 2.61 Å) were not observed clearly in the post-mortem subsamples. Additionally, a reflection at 3.03 Å was observed in the subsample next to the C-B interface; this reflection is characteristic of calcite and sharper than the reflection at 3.04-3.06 Å. The GI-XRD patterns on the surface of the low-pH cement mortar (separated by a PTFE membrane from the bentonite) showed little difference from the patterns recorded on the reference material (Fig. 10a). A subtle peak broadening and shift from 3.05 to 3.03 Å is also detected in the low fixed-angle (1°) pattern, representing a small thickness surficial cement mortar area accessible to the X-rays. SEM-EDX images and spot analyses of the same subsample showed typical calcite morphologies composed of Ca and carbon (Fig. 11a).

#### *FEBEX-bentonite perturbations*

The chemical perturbations observed in the FEBEX-bentonite have a thickness of ~ 500-600 µm from the C-B interface (Fig. 6b). The EDX compositional profile indicates a Ca increase at 20 µm from the C-B interface, in agreement with an Al depletion in the same region (Fig. 6c). Additionally, the EDX analyses showed a Mg/Si ratio of  $0.5 \pm 0.1$  (based on 8 analyses) on the surface of bentonite (Fig. 11b) in contact with only the low-pH cement mortar and  $0.2 \pm 0.05$  if the Mg/Si ratio is obtained from the first 13 analyses performed from the C-B interface on the EDX profile, representative of a thickness of 400 µm from the C-B interface. The enrichment in Mg near the cement mortar interface contrasts with the Mg/Si ratio of  $0.10 \pm 0.05$  obtained from 9 analyses far from the interface (in the range of 600-8600 µm from the C-B interface) using the same approximation.

The mineralogical data obtained by XRD and GI-XRD (Figs. 10b and 12) showed minimal changes in montmorillonite (Mnt) compared to those in the reference sample of FEBEX-bentonite. These changes are characterized by a weak decrease in the intensity of the Mnt basal reflection at 14.7 Å as the subsamples approach the C-B interface (Fig. 12). This effect was

accompanied by an increase in the background towards higher angles using the Mnt basal reflection as the reference (from 7 to 17° for  $2\theta$ ) in the subsample at 3 mm from the C-B interface.

## DISCUSSION

The FEBEX-bentonite buffer capacity is manifested according to the pH 8.3 obtained in the collected water (Table 3), very close to the pore water pH measured in the original bentonite and consistent with the exchange complex and bentonite mineral equilibria (Fernández *et al.*, 2004). Aqueous silica showed concentrations within the solubility equilibrium of quartz and cristobalite (Williams *et al.*, 1985), which are minerals present in bentonite. The dissolution of Mnt in the first microns and the precipitation of secondary phases may also have an important role with regard to the pH decrease, where the OH<sup>-</sup> consumption at the interface will prevent further alteration of bentonite (Gaucher & Blanc, 2006; Savage *et al.*, 2007). In addition to the buffer capacity, bentonite also controls the hydraulic conductivity. The FEBEX-bentonite hydraulic conductivity at room temperature (23 °C) and at a dry density of 1.6 g/cm<sup>3</sup> has been reported previously to be on the order of 10<sup>-13</sup> m/s (Villar, 2000; Villar, 2002; Villar *et al.*, 2004), in agreement with the value of hydraulic conductivity calculated in the present study (1.6×10<sup>-13</sup> m/s). This could support the pilot experimental setup validity because the advective transport regime was very low and the diffusion was relevant (Muhammad, 2004; Bourg & Tournassat, 2015), as expected in a real repository scenario. Three main chemical disturbances have been observed around the reactive interfaces in the experiment: i) decalcification of C-S-H at the C-W and C-B interfaces, ii) carbonation at the C-B interface (on the low-pH cement mortar side), and iii) Mg-perturbation in bentonite next to the C-B interface.

### *Decalcification of C-S-H*

The Ca leaching process has been mainly identified at the C-W interface. The deterioration of low-pH cement-based materials starts with Na and K dissolution followed by decalcification of the C-S-H. Although low-pH cement leaching has not been widely studied, aqueous silica is expected to remain saturated with respect to quartz. Then, Ca leaching in such a solution might

cause the formation of secondary C-S-H with a lower Ca/Si ratio than the initial C-S-H phases. Compared with the thickness of decalcification at the C-W interface (~3 mm) observed in the present experiment, an alteration thickness of 700 µm was reported in a low-pH concrete composed of Portland cement with additions of silica fume after 14 months and exposure to granitic groundwater flow (García Calvo *et al.*, 2010).

At the C-B interface, the decalcification of C-S-H may have occurred according to the lower Ca/Si ratio of the spot EDX analyses from the cement matrix ( $0.8 \pm 0.1$ ) and the C-S-H (Ca/Si = 0.6) found on the surface of the cement mortar in contact with only bentonite. These low Ca/Si ratios are close to the results provided by García Calvo (2012), and they are also consistent with leaching experiments by Baston *et al.*, 2012 with low-pH concrete under similar experimental conditions. Possible evidence for C-S-H alteration of the low-pH cement mortar was determined by means of the XRD patterns (Fig. 9a-b). Moreover, the migration of Al from bentonite next to the C-B interface could lead to the formation of metastable C-A-S-H (Pegado *et al.*, 2014); although C-A-S-H have not been identified, this migration of Al to the low-pH cement mortar due to the exchange of soluble species (Fig. 6c), together with enough sulphate content, may favour the ettringite precipitation, as suggested by the presence of needle morphologies in the EDX and SEM images from the punctual analyses. Low-pH concrete in contact with clayey rocks rich in sulphates was studied by the Cement–Opalinus Clay Interaction project (CI) experiment in Mont Terri (Dauzères *et al.*, 2016) where secondary ettringite precipitates at this interface, with this mineral being stable in the pH range of 11.0-12.5 (McCarthy *et al.*, 1991), as determined in the low-pH cement mortar in the present study.

#### *Carbonation at the C-B interface*

A carbonation process (calcite precipitation) is suggested by the SEM images (e.g., Fig. 11a) and the XRD and GI-XRD analyses (Figs. 9a-b and 10a) at the C-B interface. The dissolved CO<sub>2</sub> species could be provided by the clayey pore solutions (Dauzères *et al.*, 2014, Jenni *et al.*, 2014) mainly as HCO<sub>3</sub><sup>-</sup>, which is unstable in alkaline environments compared to CO<sub>3</sub><sup>2-</sup>. Then, these carbonates could react with the available Ca ions in the low-pH cement mortar pore solution to precipitate as CaCO<sub>3</sub> on the

cement-mortar interface. This is experimentally observed by the increase in Ca observed at the C-B interface (0-100 µm on the cement mortar side), and it is complemented by the images of the abovementioned calcite. Calcite precipitation at the interface has been observed by other authors in much longer time experiments to lead to a decrease in porosity (Cuevas *et al.*, 2014).

#### *Mg perturbation at the C-B interface*

Mg is present as an exchangeable cation in FEBEX-bentonite so that it can be readily displaced by Ca ions leached from the cement mortar pore water. In fact, the decrease of exchangeable Mg in the FEBEX-bentonite in contact with concrete has been probed in an *in situ* experiment at the Grimsel-test site (Switzerland) (Villar *et al.*, 2018). The pH > 11.0 porewater of the low-pH cement mortar is sufficient to form new mineral Mg-phases, such as brucite (pH 10.5) or Mg-silicate hydrates (M-S-H; e.g., Nied *et al.*, 2016). These Mg-rich phases have not been detected by XRD in the present study because of the narrow thickness (<500 µm), in which a slight Mg enrichment has been detected by EDX at the bentonite side of the C-B interface. Although not measured in the present study, a redistribution of the exchangeable cation population in bentonite is expected. Surface mobility may induce Mg to move from the exchange complex and precipitate in the alkaline medium. Mg perturbation at the bentonite-cement interface has been previously reported by other authors to a greater extent (Fernández *et al.*, 2010). However, those previous studies were performed over longer experimental times and under more highly alkaline conditions imposed by OPC concrete. The presence of larger amounts of Mg may expand the number of phases to be considered from brucite to brucite-intercalated Mnt and serpentine-like phases (Fernández *et al.*, 2009; Fernández *et al.*, 2013).

## CONCLUSIONS

In this study, a novel and reliable method to perform small-scale laboratory experiments concerning concrete-bentonite reactivity in a granitic DGR has been tested. Only minor reactivity has been observed. However, the following chemical perturbations have been detected in spite of the short experimental time: 1) cement mortar decalcification at the cement mortar-

bentonite and cement mortar-water interfaces, 2) slight carbonation in the low-pH cement mortar next to the interface with bentonite, and 3) Mg enrichment in bentonite at the interface with the cement mortar. These results are spatially limited but coherent with those previously observed over the long-term, either at the laboratory-scale or in large underground facilities. Presently, this experimental design is being applied to interactions of bentonite with high-pH cement mortar over longer times and using real groundwater compositions. Additional analytical techniques will be required for an improved interpretation of the results, which should provide valuable information and contribute to the knowledge of the interaction between geochemical barriers under different scenarios planned for DGR.

#### ACKNOWLEDGEMENTS

The research leading to these results has received funding from the European Union's Horizon 2020 Research and Training Programme of the EURATOM (H2020-NFRP-2014/2015) under grant agreement n° 662147 (CEBAMA). We also thank the expertise of Dr. Enrique Rodríguez Cañas in driving the SEM-EDX equipment shared for research in the Interdepartmental Research Service (SIIdI) of the Autonomus University of Madrid.

#### REFERENCES

- Bäckblom G. (2005) R&D on low-pH cement for a geological repository in: *SKB and the ESDRED project: 2<sup>nd</sup> low-pH workshop proceedings*. Enresa, Madrid, Spain.
- Bartier D., Techer I., Dauzères A., Boulvais P., Blanc-Valleron M-M. & Cabrera J. (2013) In situ investigations and reactive transport modelling of cement paste/argillite interactions in a saturated context and outside an excavated disturbed zone. *Applied Geochemistry*, **31**, 94-108.
- Baston G.M.N., Clacher A.P., Heath T.G., Hunter F.M.I., Smith V. & Swanton S.W. (2012) Calcium silicate hydrate (C-S-H) gel dissolution and pH buffering in a cementitious near field. *Mineralogical Magazine*, **76**(8), 3045–3053.
- Berner U., Kulik D. & Kosakowski G. (2013) Geochemical impact of a low-pH cement liner on the near field of a repository for spent fuel and high-level radioactive waste. *Physics and Chemistry of the Earth*, **64**, 46–56.



- 319 Bildstein O. & Claret F. (2015) Stability of barriers under chemical perturbations. Pp. 155-188 in: *Natural and Engineered Clay*  
320 *Barriers* (C. Tournassat, C.I. Steefel, I.C. Bourg & F. Bergaya, editors). Elsevier Ltd, Amsterdam.
- 321 Bourg I.C. & Tournassat C. (2015) Self-diffusion of water and ions in clay barriers. Pp. 189–226 in: *Natural and Engineered*  
322 *Clay Barriers*. (C. Tournassat, C.I. Steefel, I.C. Bourg & F. Bergaya, editors). Elsevier Ltd, Amsterdam.
- 323 Caballero E., de Cisneros C., Huertas F., Huertas F., Pozzuoli A. & Linares J. (2005) Bentonites from Cabo de Gata, Almería,  
324 Spain: a mineralogical and geochemical overview. *Clay Minerals*, **40**, 463-480.
- 325 Cuevas J., Samper J., Turrero M.J. & Wieczorek K. (2014) Impact of the Geochemical Evolution of Bentonite Barriers on  
326 Repository Safety Functions. Pp. 35-42 in: *PEBS Case 4. Proceedings International Conference on the Performance of*  
327 *Engineered Barrier: Physical and Chemical Properties, Behavior and Evolution* (BGR. A. Schäfers & S. Fahland,  
328 editors). Hannover, Germany.
- 329 Cuevas J., Ruiz A.I., Fernández R., Torres E., Escribano A., Regadío M. & Turrero M.J. (2016) Lime mortar-compacted  
330 bentonite–magnetite interfaces: An experimental study focused on the understanding of the EBS long-term performance  
331 for high-level nuclear waste isolation DGR concept. *Applied Clay Science*, **124-125**, 79-93.
- 332 Dauzères A., Le Bescop P., Sardini P. & Cau Dit Coumes C. (2010) Physico-chemical investigation of clayey/cement-based  
333 materials interaction in the context of geological waste disposal: Experimental approach and results. *Cement and Concrete*  
334 *Research*, **40**, 1327-1340.
- 335 Dauzères A., Le Bescop P., Cau-Dit-Coumes C., Brunet F., Bourbon X., Timonen J. Voutilainen M., Chomat L. & Sardini P.  
336 (2014) On the physico-chemical evolution of low-pH and CEM I cement pastes interacting with Callovo-Oxfordian pore  
337 water under its in situ CO<sub>2</sub> partial pressure. *Cement and Concrete Research*, **58**, 76-88.
- 338 Dauzères A., Achiedo G., Nied D., Bernard E., Alahrache S. & Lothenbach B. (2016) Magnesium Perturbation in low-pH  
339 Concretes Placed in Clayey Environment—Solid Characterizations and Modeling. *Cement and Concrete Research*, **79**,  
340 137-150.
- 341 ENRESA. (2006) Post-mortem bentonite analysis. Pp. 183 In: *FEBEX project final report* (M.V. Villar, editor). Publicación  
342 técnica 1-5/2006, Madrid, Spain.
- 343 Ewing R., Whittleston R. & Yardley B. (2016) Geological Disposal of Nuclear Waste: a Primer. *Elements*, **12**, 233-237.
- 344 Fernández AM., Baeyens b., Bradbury M. & Rivas P. (2004) Analysis of the porewater chemical composition of a Spanish  
345 compacted bentonite used in an engineered barrier. *Physics and Chemistry of the Earth*, **29**, 105-118.
- 346 ernández R., Fernández R., Mäder U., Rastrero M., Vigil de la Villa Mencía R. & Cuevas J. (2009) Alteration of compacted  
347 bentonite by diffusion of highly alkaline solutions. *European Journal of Mineralogy*, **21**, 725–735.
- 348 Fernández R., Mäder U. & Cuevas J. (2010) Modeling experimental results of diffusion of alkaline solutions through a  
349 compacted bentonite barrier. *Cement and Concrete Research*, **40**, 1255-1264.
- 350 Fernández R., Vigil de la Villa R., Ruiz A.I., García R. & Cuevas J. (2013) Precipitation of chlorite-like structures during OPC  
351 porewater diffusion through compacted bentonite at 90°C. *Applied Clay Science*, **83-84**, 357-367.
- 352 Fernández R., Torres E., Ruiz A.I., Cuevas J., Alonso, M.C., García Calvo, J.L., Rodríguez E. & Turrero M.J. (2017) Interaction  
353 processes at the concrete-bentonite interface after 13 years of FEBEX-Plug operation. Part II: Bentonite contact. *Physics*  
354 *and Chemistry of the Earth*, Parts A/B/C, **99**, 49–63.

- 355 Gaboreau S., Prêt D., Tinseau E., Claret F., Pellegrini D & Stammose D. (2011) 15 years of in situ cement–argillite interaction  
356 from Tournemire Characterisation of the multi-scale spatial heterogeneities of pore space evolution. *Applied*  
357 *Geochemistry*, **26**, 2159-2171.
- 358 Gaboreau S., Lerouge C., Dewonck S., Linard Y., Bourbon X., Fialips C.I., Mazurier A., Prêt d., Borschneck D., Montouillout  
359 V., Gaucher E. C. & Claret F. (2012) In-situ interaction of cement paste and shotcrete with Claystones in a deep disposal  
360 context. *American Journal of Science*, **312**, 314-356.
- 361 García Calvo J.L., Hidalgo A., Alonso C. & Fernández L. (2010) Development of low-PH Cementitious Materials for HLRW  
362 Repositories. *Cement and Concrete Research*, **40**, 1290-1297.
- 363 García Calvo J.L. (2012) *Desarrollo De Materiales de Construcción con Cemento de Bajo pH, compatibles con la Barrera de*  
364 *Ingeniería de un Almacenamiento Geológico Profundo de Residuos Radiactivos de Alta Actividad*. PhD thesis, Instituto  
365 Eduardo Torroja de Ciencias de la Construcción, Spain.
- 366 Gaucher E. & Blanc P. (2006) Cement/clay interactions – A review: Experiments, natural analogues, and modelling. *Waste*  
367 *Management*, **26**, 776-788.
- 368 Gibney E. (2015) Why Finland now leads the world in nuclear waste storage. *Nature*. doi.org/10.1038/nature.2015.18903.
- 369 Gómez-Espina R. & Villar M.V. (2016) Time evolution of mx-80 bentonite geochemistry under thermo-hydraulic gradients.  
370 *Clay Minerals*, **51**, 145-160.
- 371 IAEA-TECDOC-1718. Characterization of Swelling Clays as Components of the Engineered Barrier System for Geological  
372 Repositories. Results of an IAEA Coordinated Research Project 2002–2007.
- 373 Jenni A., Mäder U., Lerouge C., Gaboreau S. & Schwyn B. (2014) In situ interaction between different concretes and Opalinus  
374 Clay. *Physics and Chemistry of the Earth*, **70–71**, 71–83.
- 375 Kaufhold S., Dohrmann R., Sandén T., Sellin P. & Svensson D. (2013) Mineralogical investigations of the first package of the  
376 alternative buffer material test – I. Alteration of bentonites. *Clay Minerals*, **48**, 199-213.
- 377 Kaufhold S. & Dohrmann R. (2018) Distinguishing between more and less suitable bentonites for storage of high-level  
378 radioactive waste. *Clay Minerals*, **51**, 289-302.
- 379 Lerouge C., Gaboreau S., Grangeon S., Claret F., Warmont F., Jenni A., Cloet V. & Mäder U. (2017) In situ interactions between  
380 Opalinus Clay and Low Alkali Concrete. *Physics and Chemistry of the Earth*, **99**, 3–21.
- 381 Liu S., Jacques D., Govaerts J. & Wang L. (2014) Conceptual model analysis of interaction at a concrete-Boom Clay Interface.  
382 *Physics and Chemistry of the Earth*, **70–71**, 150–159.
- 383 Lothenbach B., Nied D., L'Hôpital E., Achiedo G. & Dauzères A. (2015) Magnesium and Calcium Silicate Hydrates. *Cement*  
384 *and Concrete Research*, **77**, 60-68.
- 385 Mäder U., Jenni A., Lerouge C., Gaboreau S., Miyoshi S., Kimura Y., Cloet V., Fukaya M., Claret F., Otake T., Shibata M. &  
386 Lothenbach B. (2017) 5-year chemico-physical evolution of concrete–claystone interfaces, Mont Terri rock laboratory  
387 (Switzerland). *Swiss Journal of Geosciences*, **110**, 307-327.
- 388 McCarthy G., Hassett D. & Bender J. (1991) Synthesis, Crystal Chemistry and Stability of Ettringite, A Material with Potential  
389 Applications in Hazardous Waste Immobilization. *MRS Proceedings*, **245**, 129. doi:10.1557/PROC-245-129.
- 390 Meunier A., Velde B. & Griffault L. (1998) The reactivity of bentonites: A review. An application to clay barrier stability for  
391 nuclear waste storage. Pp. 187. *Clay Minerals*, **33**, 187-193

- 392 Muhammad N. (2004) *Hydraulic, Diffusion, and Retention Characteristics of Inorganic Chemicals in Bentonite*. PhD thesis,  
393 University of South Florida, EEUU.
- 394 NEA-OECD. (2003) Engineered Barrier Systems and the Safety of Deep Geological Repositories. State-of-the art Report.  
395 OECD Publications, Paris. 70 pp.
- 396 Nied D., Enemark-Rasmussen K., L'Hopital E., Skibsted J. & Lothenbach B. (2016) Properties of magnesium silicate hydrates  
397 (M-S-H). *Cement and Concrete Research*, **79**, 323-332.
- 398 Roosz C., Grangeon S., Blanc P., Montouillout V., Lothenbach B., Henocq P., Giffaut E., Vieillard P. & Gaboreau S. (2015)  
399 Crystal structure of magnesium silicate hydrates (M-S-H): The relation with 2:1 Mg-Si phyllosilicates. *Cement and*  
400 *Concrete Research*, **73**, 228-237.
- 401 Pegado L., Labbez C. & Churakov S. V. (2014) Supporting Information for: Mechanism of aluminium incorporation into C-S-  
402 H from ab initio calculations. *Journal of Materials Chemistry A*, **2**, 3477.
- 403 Savage D., Walker C., Arthur R., Rochelle C., Oda C. & Takase H. (2007) Alteration of bentonite by hyperalkaline fluids: a  
404 review of the role of secondary minerals. *Physics and Chemistry of the Earth*, **32**, 287-297.
- 405 Savage D. (2014) An assessment of the impact of the long-term evolution of engineered structures on the safety-relevant  
406 functions of the bentonite buffer in a HLW repository. Pp. 88 in: *National Cooperative for the Disposal of Radioactive*  
407 *Waste. Technical Report 13-02* (Nagra Editor). Wettingen, Switzerland.
- 408 Stronach S.A. & Glasser F.P. (1997) Modelling the impact of abundant geochemical components on phase stability and  
409 solubility of the CaO-SiO<sub>2</sub>-H<sub>2</sub>O system at 25 °C: Na<sup>+</sup>, K<sup>+</sup>, SO<sub>3</sub><sup>2-</sup>, CT and CO<sub>2</sub><sup>3-</sup>. *Advances in Cement Resesarch*, **9**, 167S-  
410 181S.
- 411 Trotignon L., Devallois V., Peycelon H., Tiffreau H. & Bourbon X. (2007) Predicting the Long Term Durability of Concrete  
412 Engineered Barriers in a Geological Repository for Radioactive Waste. *Physics and Chemistry of the Earth*, Parts A/B/C  
413 **32 (1-7)**: 259-274.
- 414 U.S. DOE. 2014. U.S. Department of Energy. (2014) Evaluation of Options for Permanent Geologic Disposal of Spent Nuclear  
415 Fuel and High-Level Radioactive Waste, Volume I. Used Fuel Disposition Campaign. Sandia National.
- 416 Van Damme H. & Pellenq R.J.M. (2013) Chapter 14.3-cement hydrates. Pp. 801-817 In: *Developments in Clay Science* (F.  
417 Bergaya, G. Lagaly, editors.). Elsevier Ltd, Amsterdam.
- 418 Villar M.V. (2000) *Caracterización termohidro-mecánica de una bentonita de Cabo de Gata*. PhD thesis, Universidad  
419 Complutense de Madrid, Spain.
- 420 Villar M.V. 2002 Thermo-hydro-mechanical characterisation of a bentonite from Cabo de Gata. Pp 285 in: *A study applied to*  
421 *the use of bentonite as sealing material in high level radioactive waste repositories*. Technical publication. ENRESA  
422 01/2002, Madrid, Spain.
- 423 Villar M.V. & Lloret A. (2004) Influence of temperature on the hydro-mechanical behaviour of a compacted bentonite. *Applied*  
424 *Clay Science*, **26**, 337-350.
- 425 Villar M.V., Martín P.L., Bárcena I., García-Siñeriz J.L., Gómez-Espina R. & Lloret A. (2012) Long-term experimental  
426 evidences of saturation of compacted bentonite under repository conditions. *Engineering Geology*, **149**–150, 57-69.
- 427 Villar M.V., Fernández A.M., Romero E., Dueck A., Cuevas J., Plötze M., Kaulhold S., Dohrman R., Iglesias, R.J., Sakaki T.,  
428 Zheng L., Kawamoto K., Kober F. (2018) FEBEX-DP Postmortem THM/THC. *Analysis Report*. Pp 142. Nagra NAB 16-  
429 017. under review.

430 Williams L.A., Parks G.A. & Crerar D.A. (1985) Silica Diagenesis, I. Solubility Controls. *SEPM Journal of Sedimentary*  
431 *Research*, **55**, 0301-0311.  
432  
433

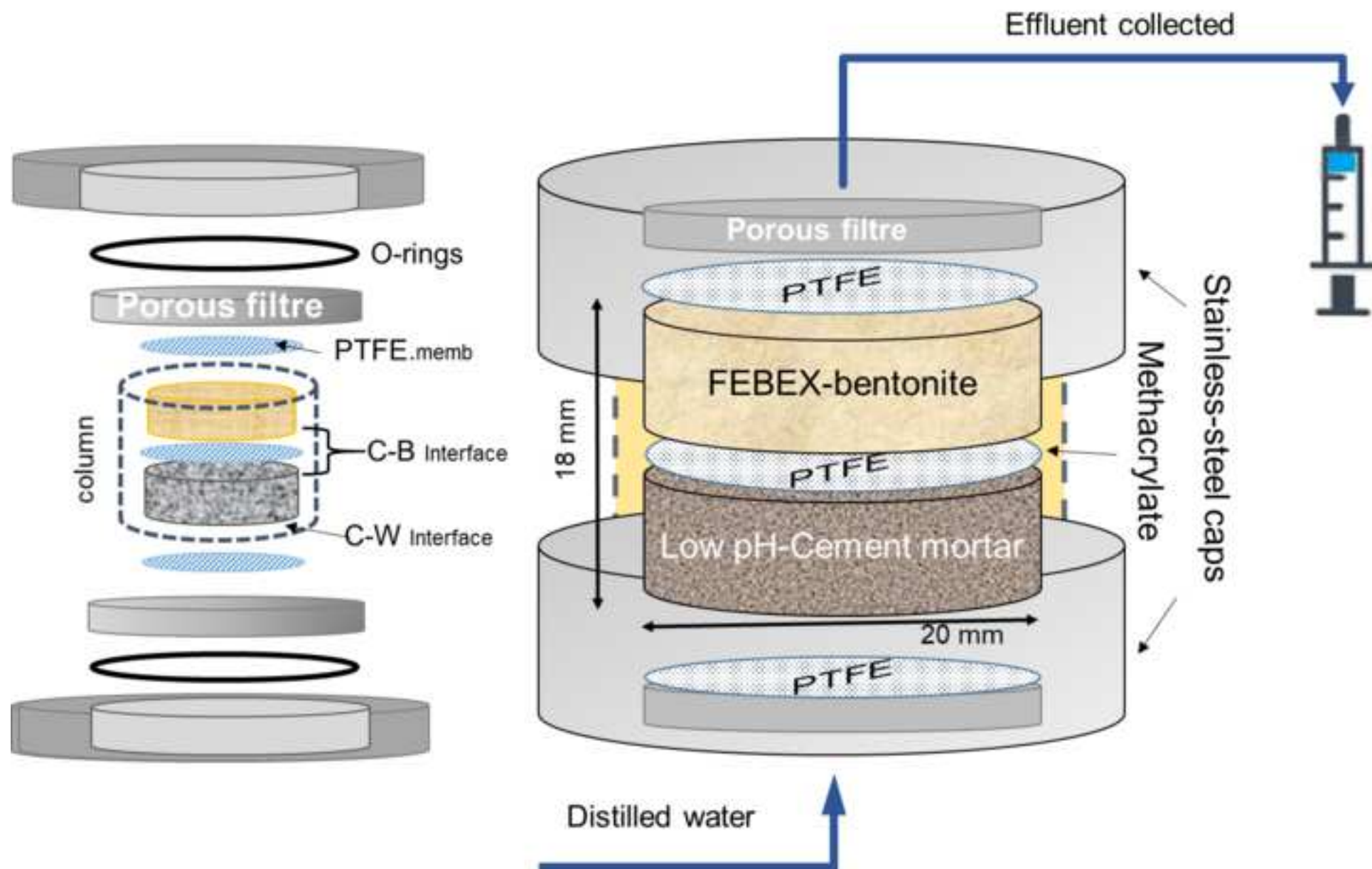
## LIST OF FIGURES

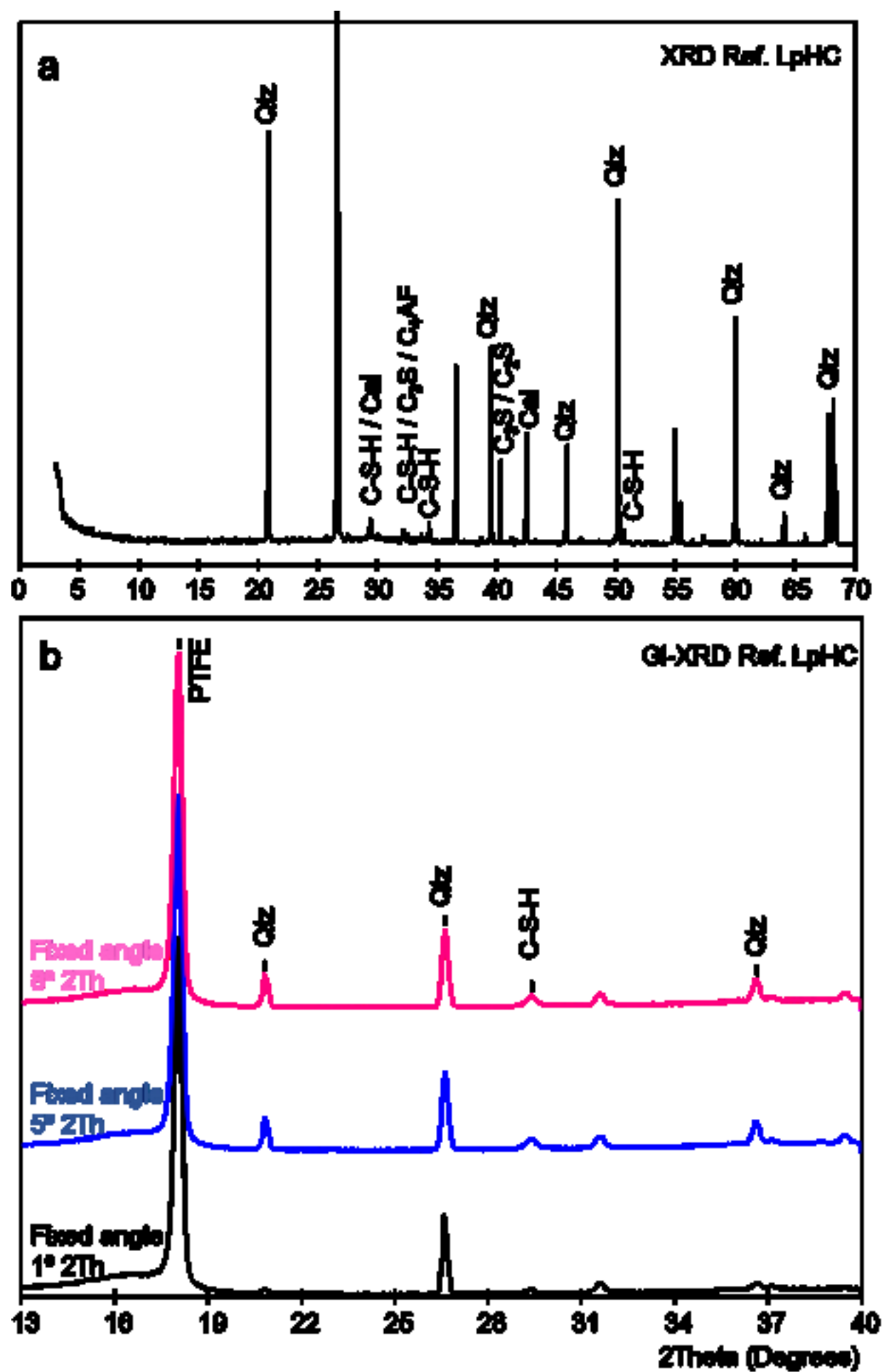
- FIG. 1. Compacted column formed from cement mortar and compacted bentonite. Both materials are separated by a PTFE membrane and encased in an open stainless-steel sleeve. A methacrylate piece seals the column. Two porous filters allow water transport at both column ends. C-B interface: cement mortar-bentonite interface; C-W interface: cement-water interface.
- FIG. 2. (a) XRD of the reference low-pH cement mortar (ref. Low-pHC). (b) GI-XRD patterns with fixed angles of  $8^\circ$ ,  $5^\circ$ , and  $1^\circ$  for  $2\theta$  of the initial-reference low-pH cement mortar. Qtz: quartz. Cal: calcite.  $C_3S$ : tricalcium silicate.  $C_4AF$ : tetracalcium aluminoferrite. C-S-H: calcium silicate hydrates.  $C_2S$ : dicalcium silicate. PTFE: polytetrafluoroethylene. Reflexions are shown in Å.
- FIG. 3. (a) Detail of SEM-EDX spots analysed in the initial-reference low-pH cement mortar to calculate the Ca/Si ratio in the cement matrix. (b) Presence of ettringite in local regions of the initial-reference low-pH cement mortar. Six spot analyses are depicted.
- FIG. 4. Cutting and sampling scheme. (a) Front view where the cement mortar-bentonite interface (C-B interface) and the cement mortar-water interface (C-W interface) have been drawn. (b) Plan view of the cement mortar-bentonite column. (c) Subsample segmentation for XRD and punctual SEM-EDX analyses performed on the surface of the subsamples next to the C-B and C-W interfaces. (d) Sample for SEM-EDX profile analyses and punctual SEM-EDX analyses near the C-B and C-W interfaces.
- FIG. 5. Backscattered electron (BSE) images showing an overview of the methodology used to create the SEM-EDX profile of the elemental compositions in the cement mortar-bentonite column. Note the increasing magnification at the interface region.
- FIG. 6. EDX profile of the column at different scales: (a)  $1000\text{ }\mu\text{m}$ , (b)  $600\text{ }\mu\text{m}$ , and c)  $100\text{ }\mu\text{m}$ . Notice that bentonite is shown on the left side and low-pH cement mortar (Low-pHC) on the right side of the figure.
- FIG. 7. (a) Detail of the SEM-EDX spots analysed in the cement matrix of the low-pH cement mortar near the C-W interface and (b) spots analysed in the cement matrix of the low-pH cement mortar near the C-B interface.
- Fig. 8. Backscattered electron (BSE) images: (a) C-S-H present on the low-pH cement mortar side next to bentonite. (b) Ettringite present on the low-pH cement mortar side next to bentonite.
- Fig. 9. (a) XRD of the reference low-pH cement mortar (Ref. LpHC) sample and reacted subsamples at 9, 6 and 3 mm from the cement mortar-bentonite interface. (b) Magnification of the complete diffractogram in the range of  $28\text{--}35$  for  $2\theta$ . Qtz: quartz, C-S-H: calcium silicate hydrates, and Cal: calcite. Reflexions are expressed in Å.
- FIG. 10. (a) GI-XRD pattern recorded for the reference low-pH cement mortar (Ref. LpHC) and the surface of the sample exposed to bentonite after the

experiment. (b) conventional XRD random powder pattern recorded for the reference FEBEX-bentonite and GI-XRD for the surface of the sample exposed to low-pH cement mortar after the experiment. PTFE: polytetrafluoroethylene, Mnt: montmorillonite, Qtz: quartz, Crs: cristobalite; Crs-Trd: cristobalite-tridymite; Pl: plagioclase, and Cal: calcite. The figures in the peaks are in units of Å.

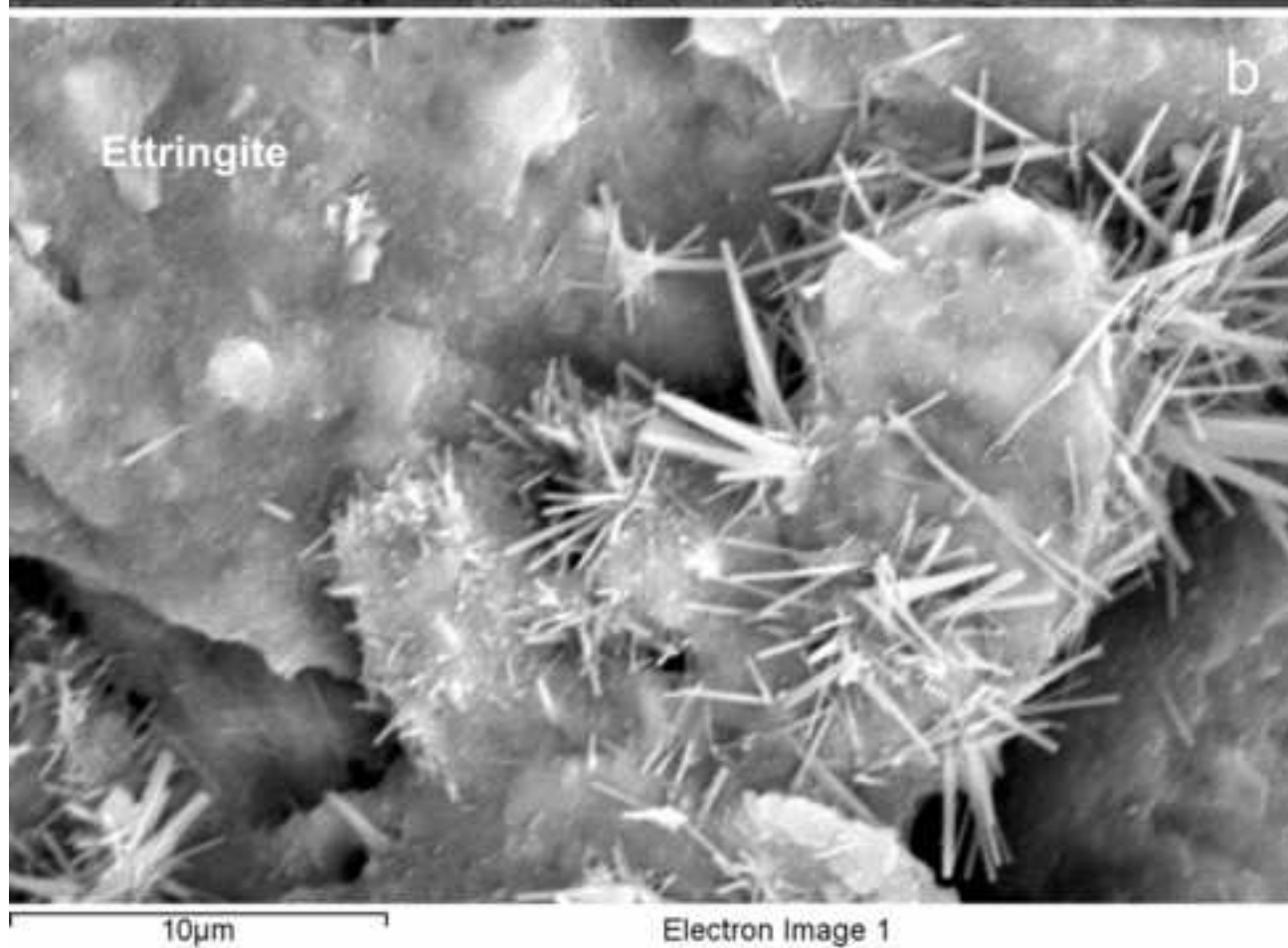
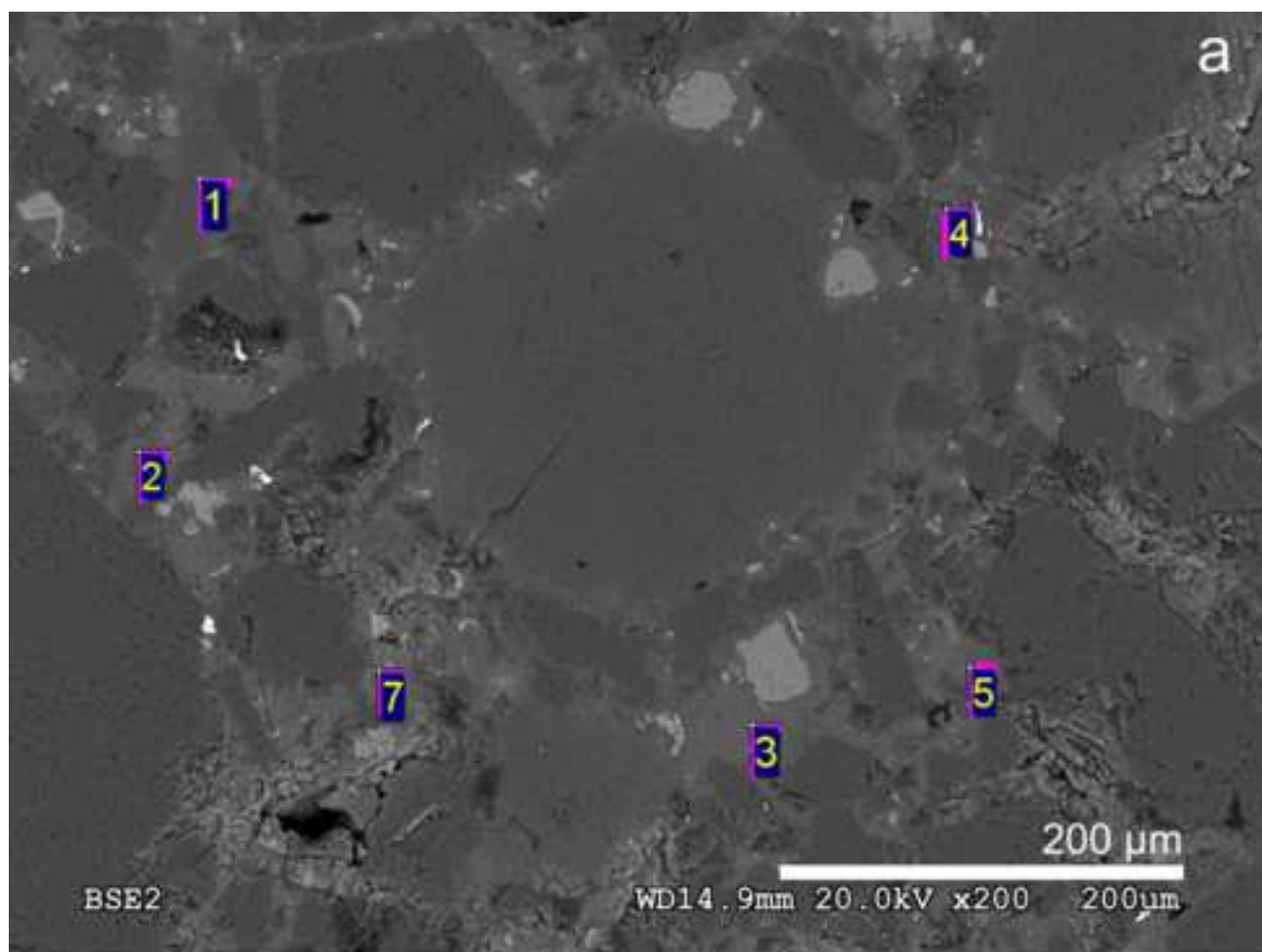
- FIG. 11. (a) Backscattered electron (BSE) image of calcite present in the low-pH-cement mortar side near the interface with bentonite. (b) Backscattered electron image of the bentonite surface exposed to cement mortar. Four EDX analyses are depicted.
- Fig. 12. FEBEX-bentonite XRD pattern. The reference FEBEX-bentonite is shown together with the overlapping subsamples at 9, 6 and 3 mm from the C-B interface. Mnt: montmorillonite. Ilt: illite. Qtz: quartz. Fsp: feldspar. Cal: calcite. Reflexions are shown in Å

Figure 1









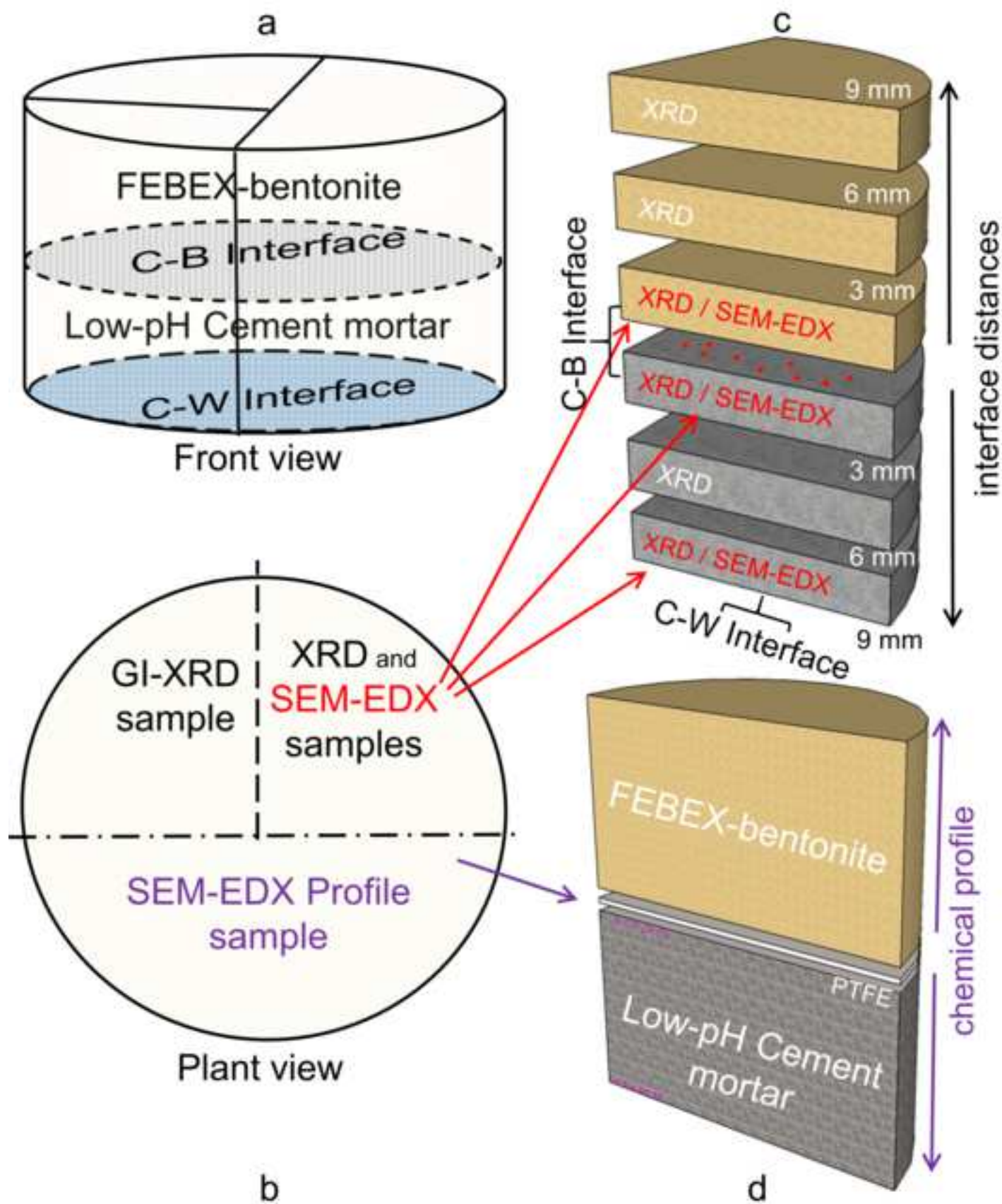
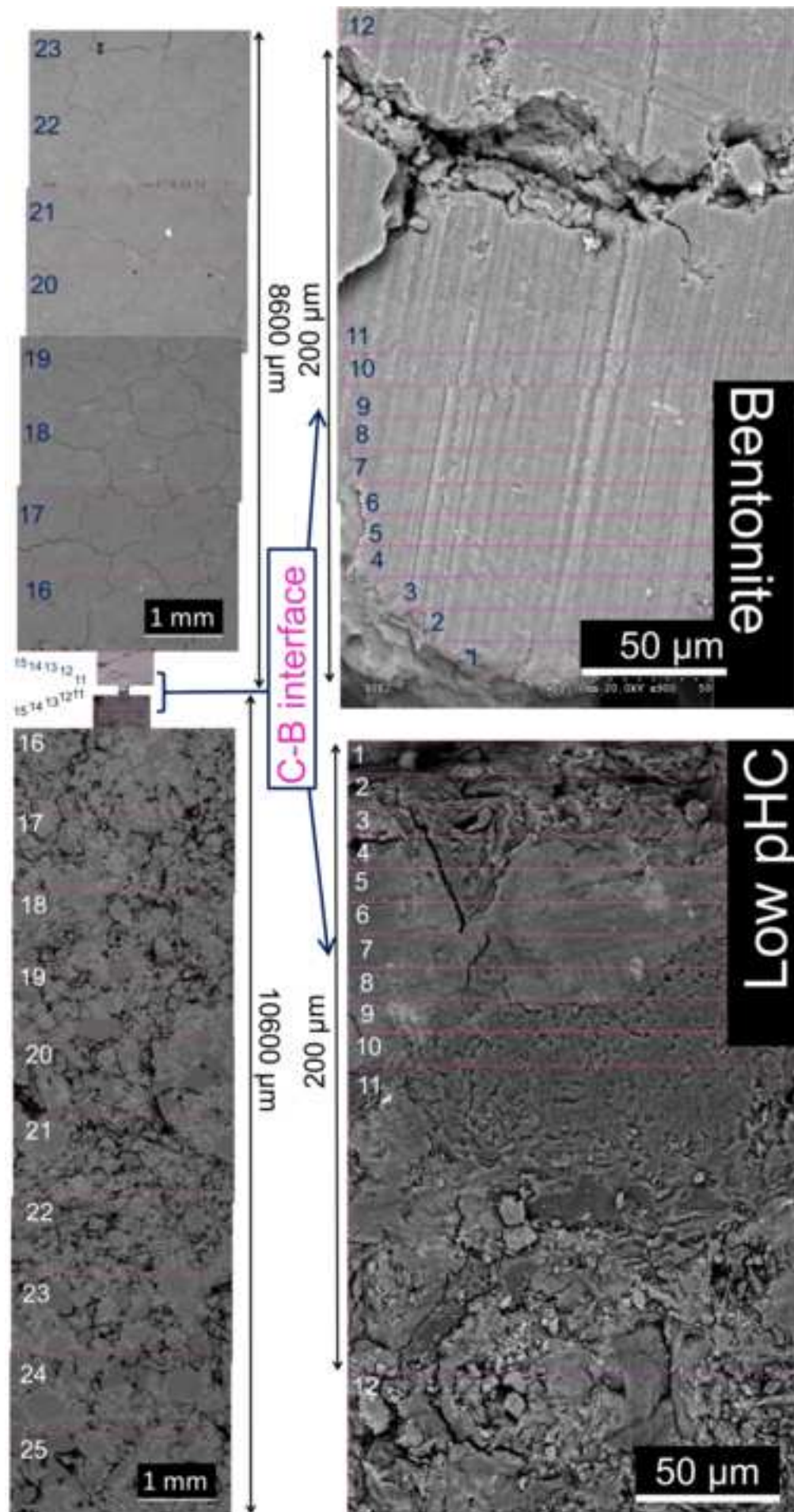
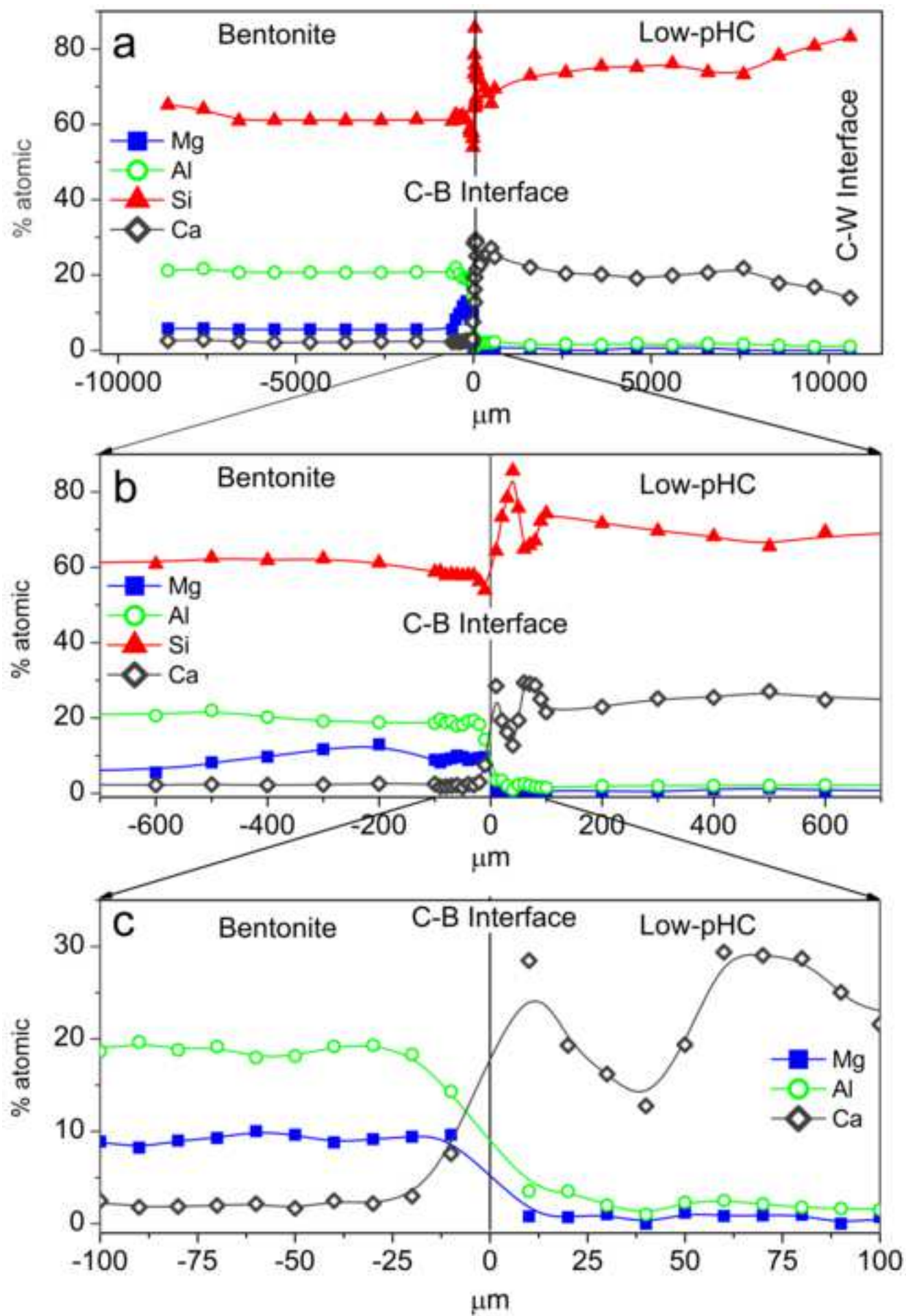


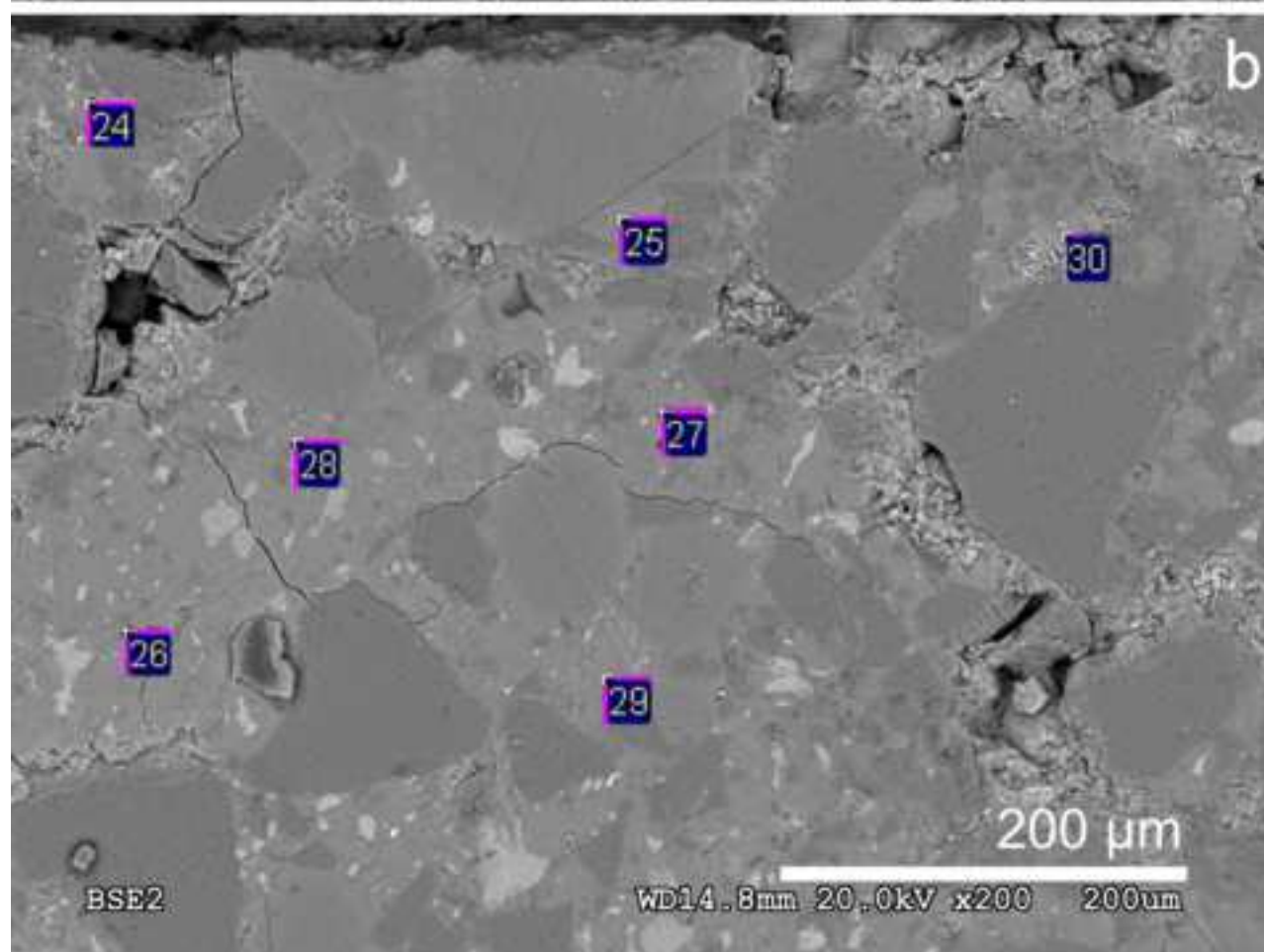
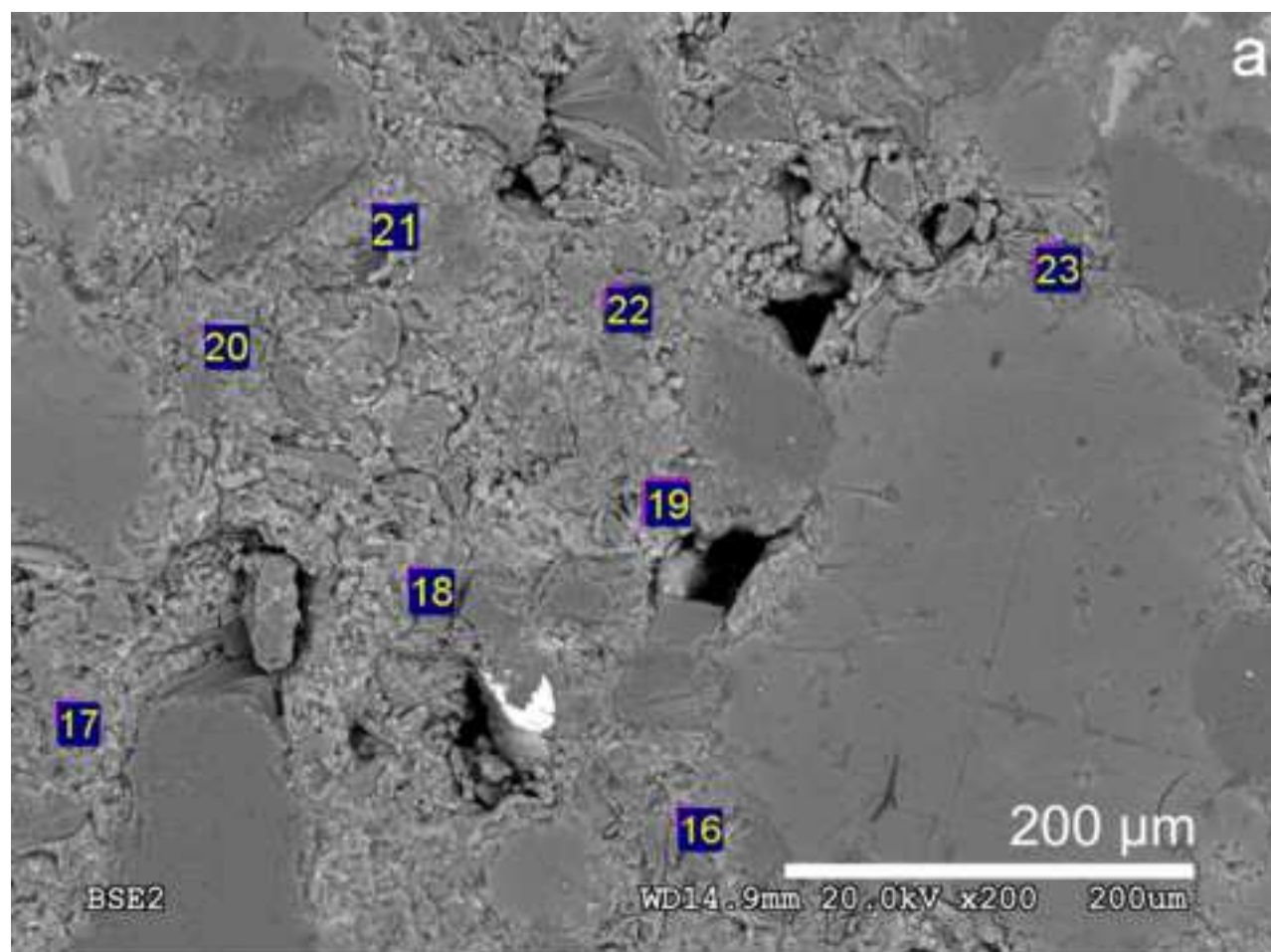


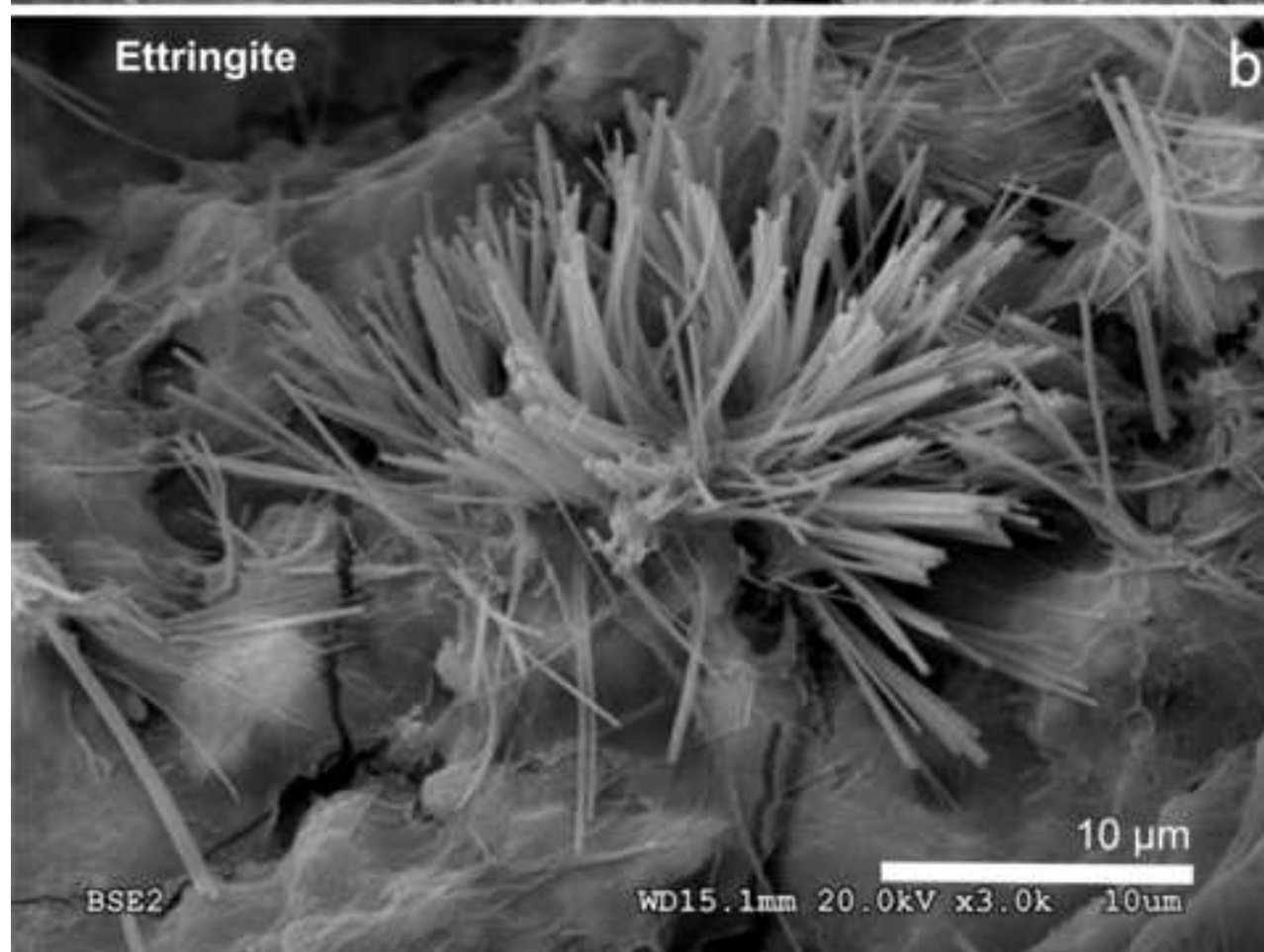
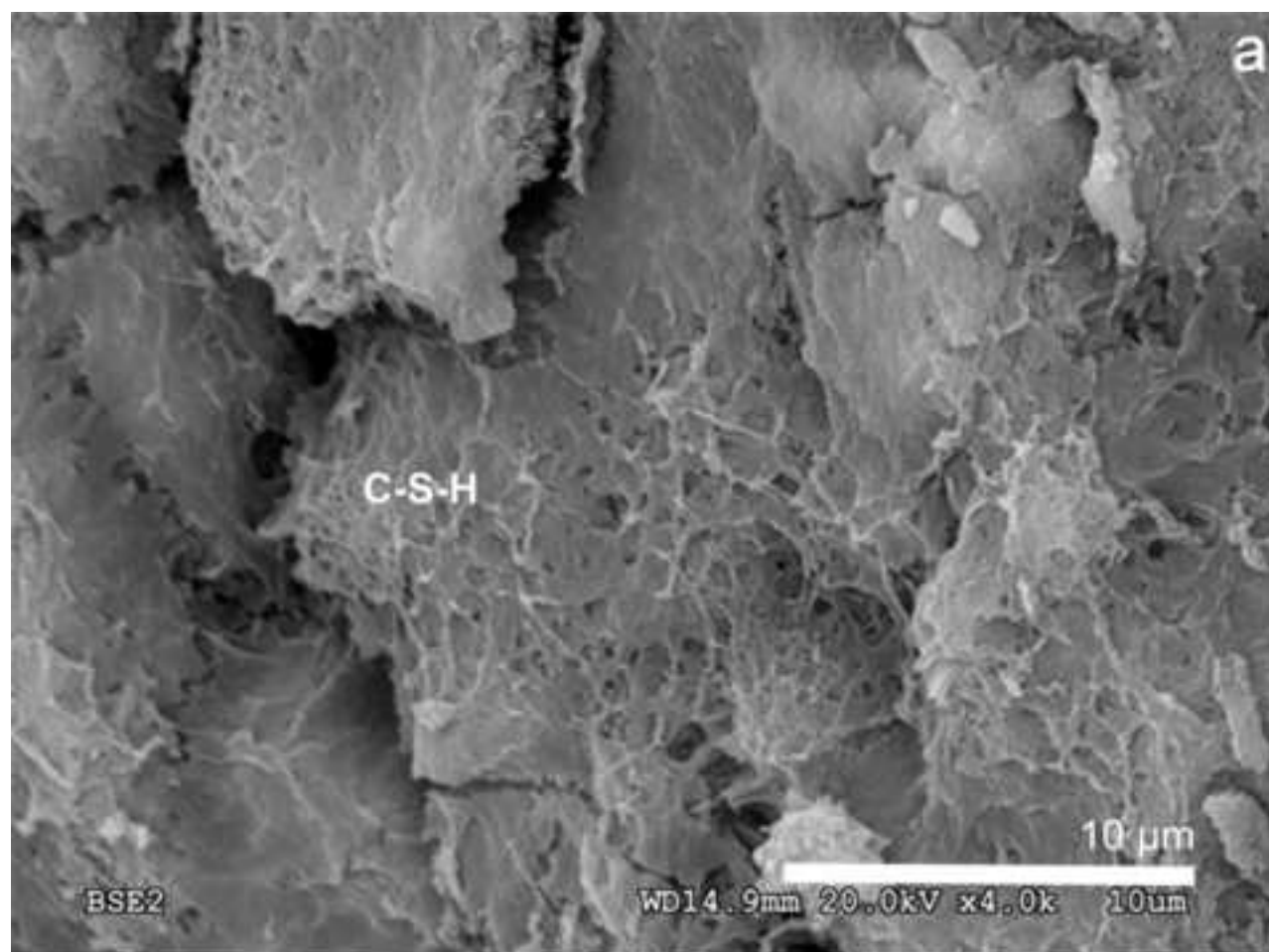
Figure 5



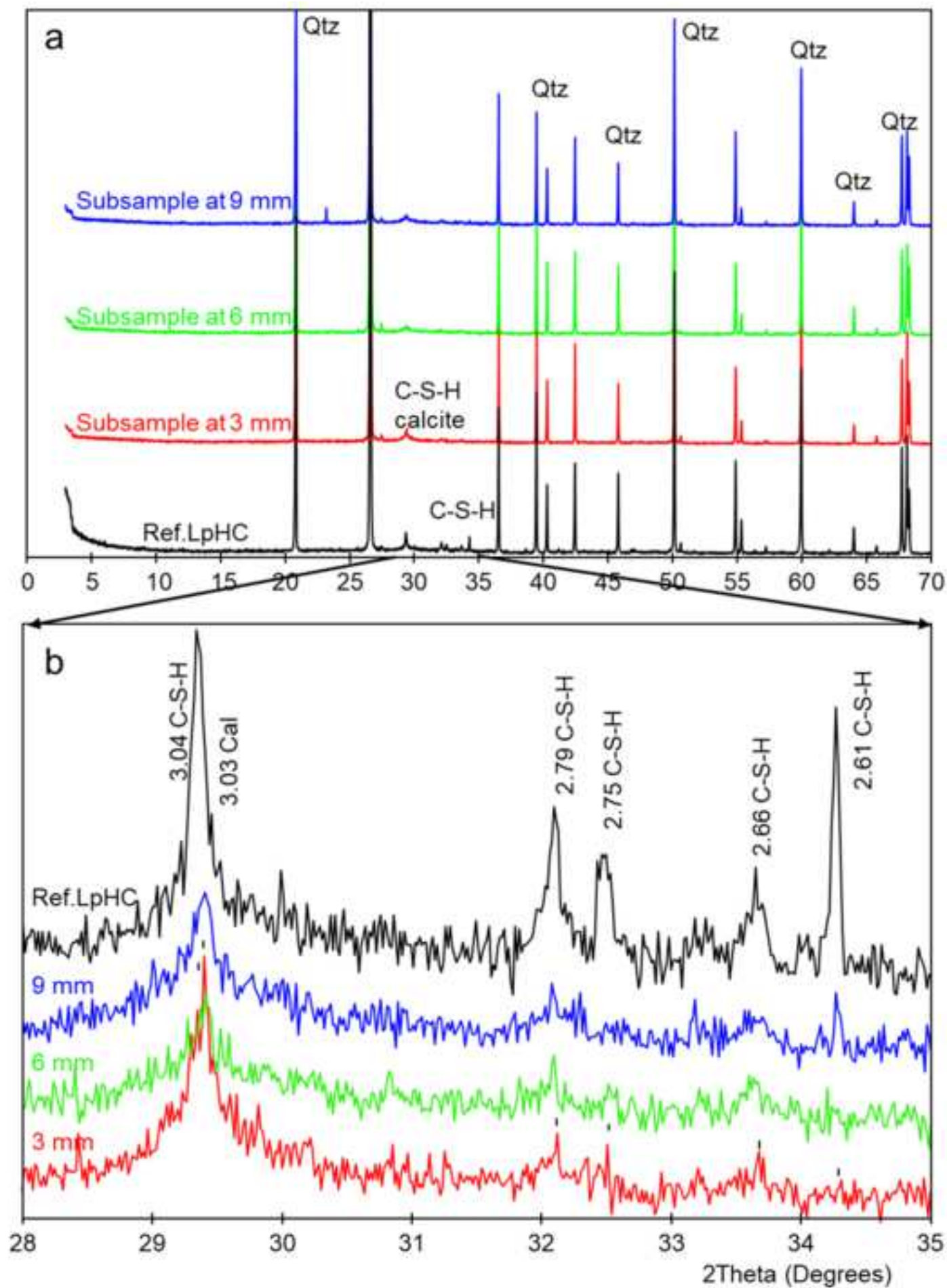


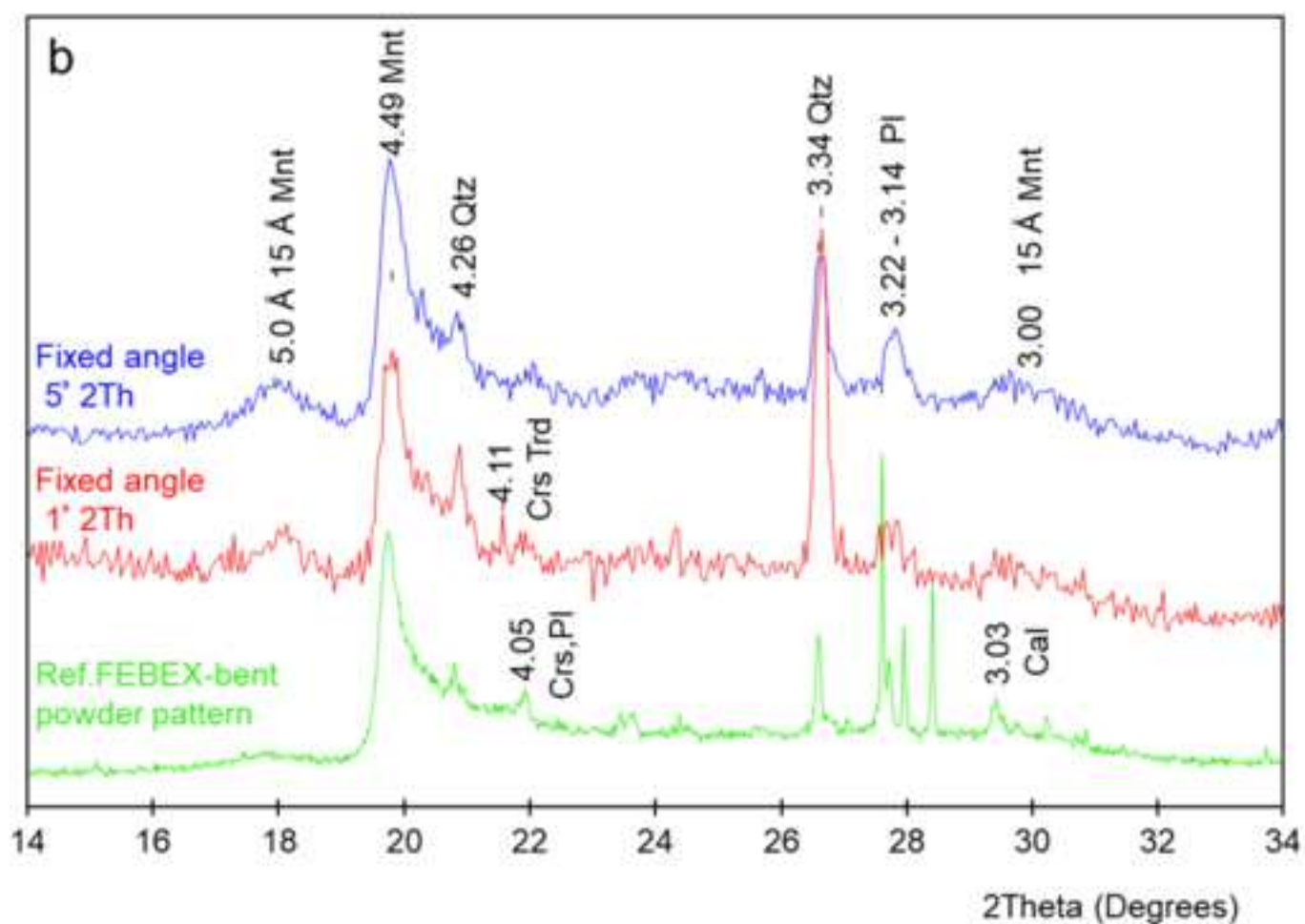
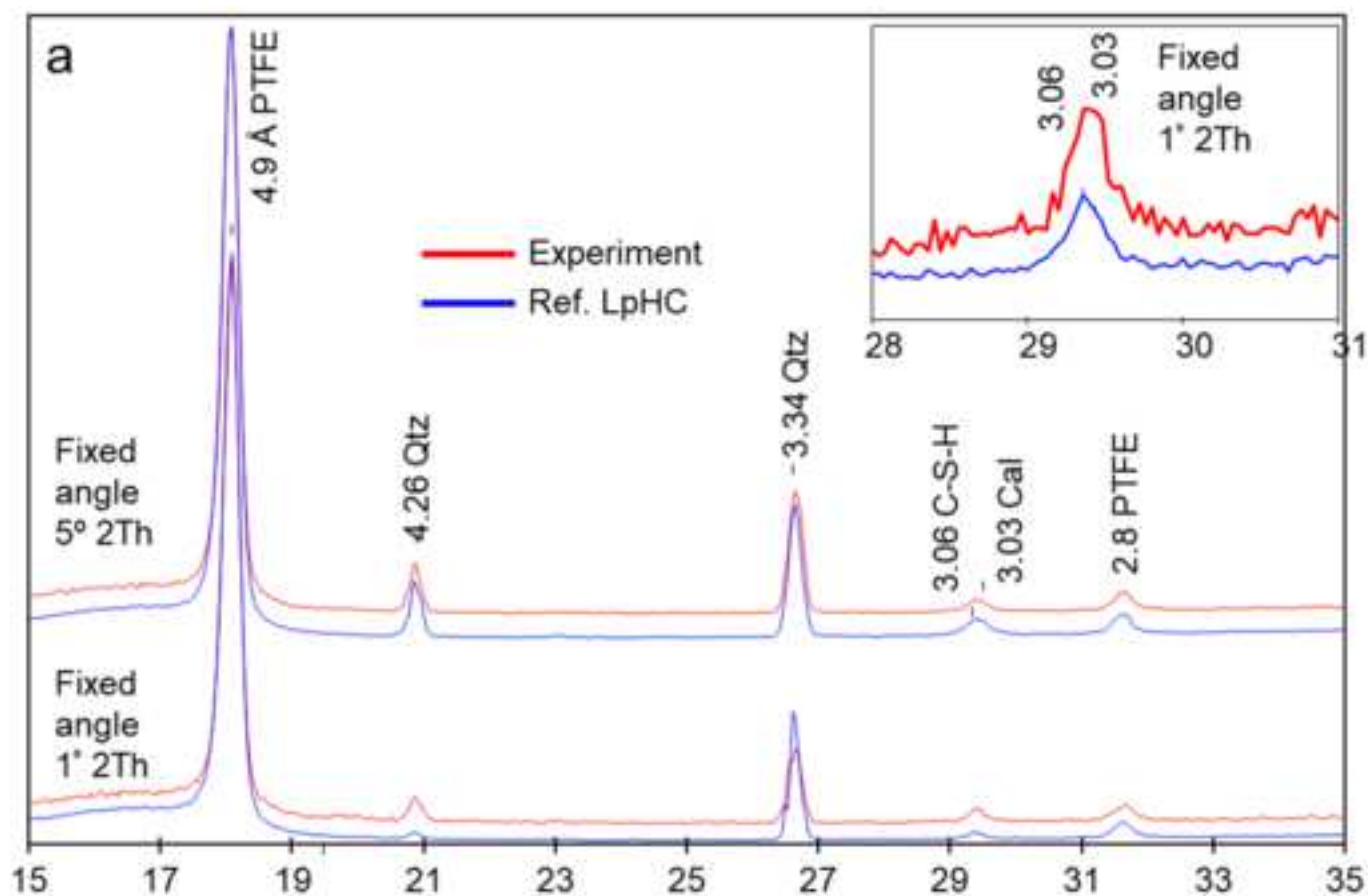














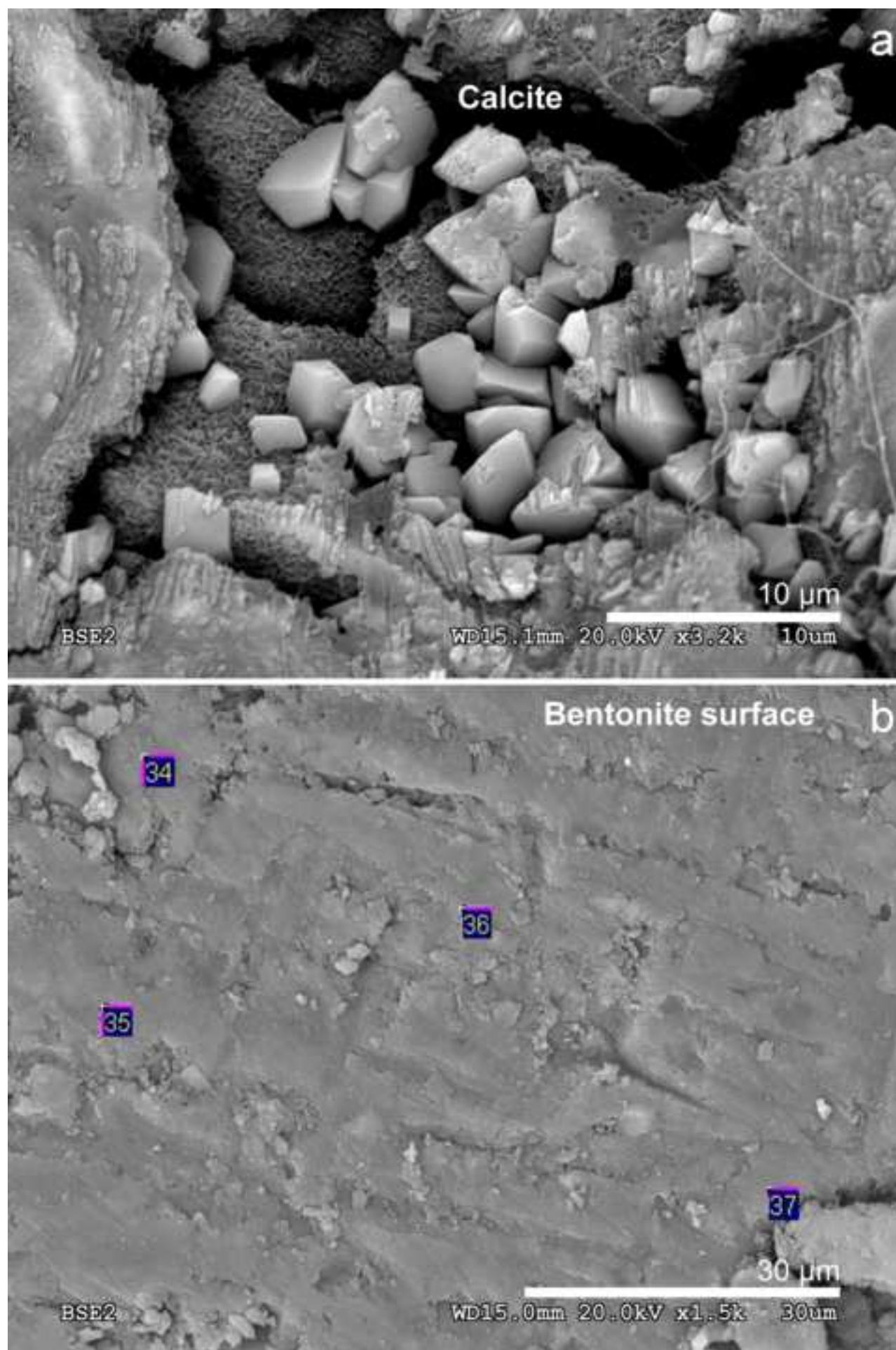
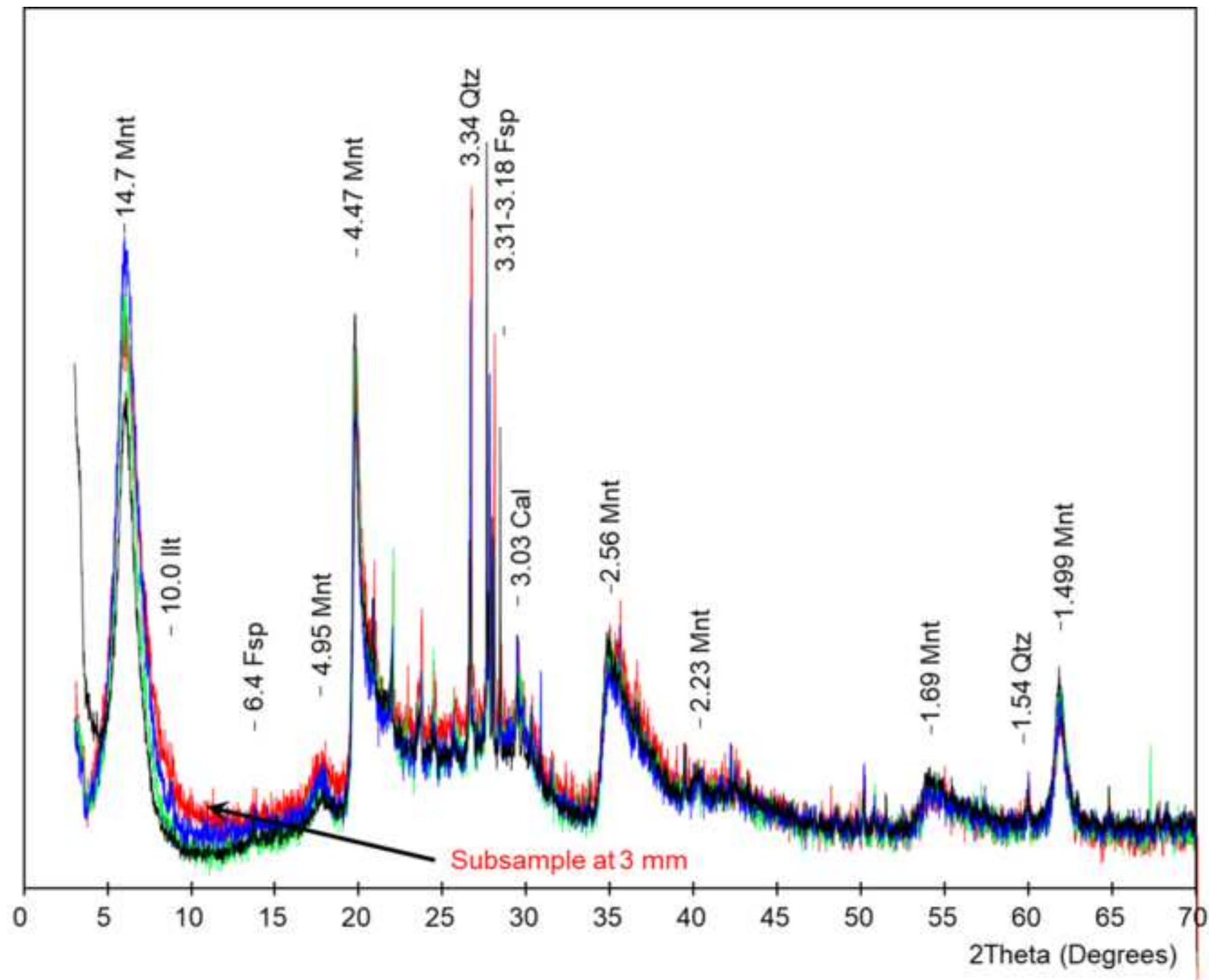


Figure 12



## LIST OF TABLES

- TABLE 1. Relative error evaluation of SEM-EDX determined chemical element concentrations.
- TABLE 2. OPC (ordinary Portland cement) and SF (silica fume) chemical composition (García Calvo, 2012).
- TABLE 3. Major ions, alkalinity, aqueous silica and pH in the effluent and chemical composition of a reference low-pH cement mortar (LpHC) pore solution (90 days of age) provided by García Calvo (2012).

Element	% element 40s*	% ID 10s-80s**	Average ID % 30s-50s	Average MD % 30s-50s
Al	5.9	17-7.0	9.0	6.0
Si	69.2	6.5-2.3	0.8	3.2
Ca	18.0	9.0-3.2	1.9	4.5
Ettringite $\text{Ca}_6\text{Al}_2(\text{SO}_4)_3(\text{OH})_{12} \cdot 26\text{H}_2\text{O}$			Ca/S Theoretical=2.0	Al/S Theoretical=0.7
Example***				
Al	16.0	5.8	1.8	0.6
Si	6.6	10.5		
S	26.9	4.5		
Ca	48.8	2.9		
Fe, Mg	< 0.2	50-75		

\*The selected integration time to determine any SEM-EDX measurement was 40 s. The element % is referenced to the sum of the major analysed elements, excluding C and O (normally, the sum of Mg, Al, Si, K, S, Ca, and

Fe)

\*\*Deviation data are expressed as a percentage given by the ratio of the standard deviation to the value determined using either the instrumental standard deviation of the integrated signal counts (ID: instrumental deviation) or the average value of several measurements (MD: measurement deviation).

\*\*\*Analyses for ettringite are described in Fernández et al., 2017.

Weight %	OPC	SF
SiO <sub>2</sub>	17.4	92.7
Al <sub>2</sub> O <sub>3</sub>	4.68	0.60
Fe <sub>2</sub> O <sub>3</sub>	5.08	5.38
total CaO	60.3	1.31
MgO	1.78	0.93
SO <sub>2</sub>	3.17	-
Na <sub>2</sub> O	0.18	0.15
K <sub>2</sub> O	0.34	0.37
Free CaO	1.85	0.01

Ion/aqueous species	Effluent (mg/L)	LpHC(mg/l)
Ca <sup>2+</sup>	93.2	612
Mg <sup>2+</sup>	2.2	nd
Na <sup>+</sup>	211.1	120
K <sup>+</sup>	2.73	322
NO <sub>3</sub> <sup>-</sup>	3.9	nd
Cl <sup>-</sup>	187.3	nd
F <sup>-</sup>	2.2	nd
SO <sub>4</sub> <sup>2-</sup>	176.2	84.4
HCO <sub>3</sub> <sup>-</sup>	237.9	nd
SiO <sub>2 (aq)</sub>	12.8	nd
pH	8.3	11.1

Nd: not determined

TABLE S1. Analyses performed at different places of the sample

<div>(%) atomic</div>												
	N° analyse	Mg	Al	Si	S	K	Ca	Fe	Ca/Si	Al/S	Mg/Si	Mineral aggregates
ref. low-pHC	1	0.0	0.4	40.6	29.5	0.0	29.5	0.0	0.7			cement matrix
	2	2.2	3.2	42.1	1.4	0.0	47.5	3.7	1.1			cement matrix
	3	0.7	0.0	53.3	0.8	0.7	44.5	0.0	0.8			cement matrix
	4	0.7	2.1	50.5	1.5	0.0	44.0	1.3	0.9			cement matrix
	5	3.5	6.7	39.4	2.9	0.0	37.4	10.1	0.9			cement matrix
	6	0.0	0.7	50.2	1.5	0.0	46.0	1.7	0.9			cement matrix
	7	0.0	0.6	54.9	0.0	0.0	44.5	0.0	0.8			cement matrix
	8	0.0	0.0	56.3	0.0	0.0	43.7	0.0	0.8			cement matrix
	9	0.0	2.0	52.0	3.4	0.0	41.1	1.5	0.8			cement matrix
	10	1.0	3.0	51.6	2.4	2.1	38.7	1.2	0.7			cement matrix
	11	1.3	2.5	53.7	0.9	0.0	40.2	1.8	0.7			cement matrix
	12	1.0	3.6	46.5	2.7	0.0	44.1	2.1	0.9			cement matrix
	13	1.2	1.7	43.0	3.7	0.0	47.5	2.9	1.1			cement matrix
	14	0.9	1.3	52.3	1.3	0.0	42.8	1.3	0.8			cement matrix
C-W Interface	* $\bar{Y} \pm S$								0.9±0.1			
	15	1.2	4.4	34.0	5.7	0.0	50.8	3.7	-	0.8		ettringite
	16	3.7	2.3	47.5	1.1	0.0	42.9	2.5	0.9			cement matrix
	17	2.3	2.2	50.5	1.6	0.0	40.8	2.6	0.8			cement matrix
	18	2.3	4.2	49.9	2.0	0.3	36.6	4.7	0.7			cement matrix
	19	1.6	2.7	48.1	2.6	0.0	43.0	2.0	0.9			cement matrix
	20	0.0	1.7	60.9	0.5	0.0	39.1	1.7	0.6			cement matrix
	21	0.0	0.0	62.2	0.0	0.0	37.8	0.0	0.6			cement matrix
	22	1.2	2.5	52.5	2.5	0.0	41.3	0.0	0.8			cement matrix
	23	0.0	0.0	63.1	0.0	0.0	36.9	0.0	0.6			cement matrix
C-B Interface	$\bar{Y} \pm S$								0.7±0.1			
	24	0.8	2.8	56.0	0.0	0.4	38.4	1.5	0.7			cement matrix
	25	2.1	1.4	49.1	0.0	0.0	45.6	1.8	0.9			cement matrix
	26	0.0	1.4	52.7	0.0	0.0	44.1	1.9	0.8			cement matrix
	27	1.2	2.2	49.3	1.0	0.0	44.1	2.1	0.9			cement matrix
	28	0.9	1.8	60.7	2.3	0.0	32.9	1.5	0.5			cement matrix
	29	3.3	3.3	50.4	0.6	0.0	39.1	3.3	0.8			cement matrix
	30	0.6	2.5	54.0	3.0	0.0	38.8	1.1	0.7			cement matrix



Surface Bentonite	$\bar{Y} \pm S$				$0.8 \pm 0.1$						
	31	5.2	1.5	58.4	0.0	0.0	34.2	0.6	0.6		C-S-H
	32	2.8	8.1	25.6	12.7	0.0	43.5	7.3	-	0.6	ettringite
	33	3.3	43.0	0.6	0.0	46.6	3.3	0.0	-		calcite
	34	25.5	15.6	54.1	0.0	1.2	1.1	2.4		0.5	**Mnt-Mg
	35	29.4	10.7	54.9	4.9	0.0	0.0	0.0		0.5	Mnt-Mg
	36	29.7	6.8	60.5	0.0	0.7	0.6	1.6		0.5	Mnt-Mg
	37	37.2	10.1	49.0	0.0	1.0	0.8	1.9		0.8	Mnt-Mg
	38	23.7	16.9	52.5	0.0	1.4	1.6	1.4		0.5	Mnt-Mg
	39	28.1	16.1	52.8	0.0	0.6	0.8	1.5		0.5	Mnt-Mg
	40	32.7	13.6	50.3	0.0	0.8	0.8	1.8		0.7	Mnt-Mg
	41	19.9	18.7	54.8	0.0	1.4	1.1	2.8		0.4	Mnt-Mg
$\bar{Y} \pm S$				$0.5 \pm 0.1$							

\* $\bar{Y} \pm S$ : arithmetic mean  $\pm$  standar deviation

\*\*Mnt-Mg: Montmorillonite rich in magnesium